Chemical Engineering Journal 450 (2022) 137865

Contents lists available at ScienceDirect

Chemical Engineering Journal

journal homepage: www.elsevier.com/locate/cej

Evaluating catalytic (gas–solid) spectroscopic cells as intrinsic kinetic reactors: Methanol-to-hydrocarbon reaction as a case study

José Valecillos [a,*], Gorka Elordi [a], Mengmeng Cui [b], Andrés T. Aguayo [a], Pedro Castaño [a,b,*]

[a] Department of Chemical Engineering, University of the Basque Country (UPV/EHU), PO Box 644, Bilbao 48080 Spain
[b] Multiscale Reaction Engineering, KAUST Catalysis Center (KCC), King Abdullah University of Science and Technology (KAUST), Thuwal 23955-6900 Saudi Arabia

ARTICLE INFO

Keywords:
Zeolite catalysis
Operando spectroscopy
Spectro-kinetics
Computational fluid dynamics
Continuously stirred tank reactor (CSTR)

ABSTRACT

Commercial spectroscopic gas–solid cell reactors are routinely used to analyze the dynamics of the catalyst (catalyst pelletized as a disc) structure and retained/adsorbed species using multiple operando techniques. These instruments have revolutionized the understanding of many catalytic reactions, including the methanol-to-hydrocarbon reactions. We propose a reaction engineering framework to evaluate spectroscopic cells based on (a) analyzing the fluid dynamic performance, (b) comparing their performance with a reference packed-bed reactor, and (c) the assessment of the external and internal mass transfer limitations. We have used a Specac HTHP and a Linkam THMS600 cell reactors coupled with the corresponding gas conditioning, spectroscopic, and mass spectrometry apparatuses. Our results reveal that these cells approach a perfect mixing only with several equivalent tanks in series and they are reliable at low catalyst loadings (thin disc) and high flowrates (low spacetimes). Under these conditions, we can avoid external-internal mass transfer limitations and fluid dynamic artifacts (e.g., bypassing or dead/stagnant volume zones), obtaining intrinsic kinetics with the corresponding operando spectroscopic signatures. The proposed methodology allows to understand the influence of process parameters and potential design modifications on the observed kinetic performance.

1. Introduction

Operando or in situ spectroscopy has transformed how we observe and analyze catalytic reactions and surfaces under working conditions [1–7]. One reaction that has been immensely affected by these methods is the catalytic methanol-to-hydrocarbons/olefins (MTH/MTO) reaction, which is a promising route to obtain petrochemicals and fuels from renewable sources using microporous-acidic catalysts [8–11]. The use of operando spectroscopy partnering with ab initio calculations has revealed steps of initiation, autocatalysis, and deactivation [12–19] during MTH/MTO reactions. In brief, acid sites are prone to form methoxy and carbocation species that dehydrate, oligomerize or alkylate/dealkylate (methylate), cyclize, and aromatize to form a whole range of products, including deactivating species [20–29]. Thus, the active site is the combination of the acid site and the adsorbed carbocation. These species undergo sequenced methylation and aromatization up to a point where the reaction rate starts to lower down or even deactivate the catalyst: As for Zeolite Socony Mobil–5 (ZSM-5), the turning point happens for the hexamethyl benzene [23].

Although no consensus exists regarding the meaning and differences of the terms “in situ” or “operando,” many authors favor the following categorization [30,31]: “in situ” focuses on the catalyst surface during the reaction, whereas “operando” covers the catalytic surface and simultaneous analysis of products derived from the reaction [32]. Thermogravimetric analysis, microscopy, and spectroscopy are the most-used techniques for in situ or operando reaction systems. In MTH reactions, the most common methods include Fourier-transform infrared (FTIR), ultraviolet–visible (UV–vis), and ^{13}C solid-state nuclear magnetic resonance (NMR) spectroscopies [33–39].

In an in situ or operando reaction, the systems consist of a cell or reactor that enables reaching the reaction conditions for the temperature, pressure, and contact. Given the applications in where they are used, most of them are for gas–solid or liquid–solid interphases. As necessary, they require several modifications to allow the spectroscopic technique to reach the catalyst surface. The spectroscopic technique and cell modifications superimpose certain limitations in the reaction conditions (e.g., the windows or walls of the cell must allow the transmission of electromagnetic radiation while withstanding the required pressures to mimic reaction conditions). Given the high demand for these reactors, commercial cells can be used in commercial microscopes or spectrometers. Companies offer long-standing knowledge, supplies,

* Corresponding authors.
E-mail addresses: jose.valecillos@ehu.eus (J. Valecillos), pedro.castano@kaust.edu.sa (P. Castaño).

https://doi.org/10.1016/j.cej.2022.137865
Received 4 May 2022; Received in revised form 27 June 2022; Accepted 29 June 2022
Available online 2 July 2022

Nomenclature

A	catalyst disc surface area
Bo	Bodenstein dimensionless number
C_p	specific heat capacity
$D_{i,m}$	mass diffusion coefficient for species i in the mixture
$D_{T,i}$	thermal diffusion coefficient
E	total energy of the fluid
$E(\theta)$	normalized residence time distribution
F_{M0}	weight or carbon-based molar flowrate of methanol in the feed
F_i	molar flow rate of component i
F_{W0}	weight flowrate of water in the feed
h	enthalpy
J_j	diffusion flux
k	heat conductivity
k_i	kinetic coefficient
k_c	molar concentration mass transfer coefficient
k_d	deactivation coefficient
$\dot{n}_M$	molar flow rate of reactant that reacts or is transferred
N	number of equivalent well-mixed equal size reactors connected in series
p	pressure
P_{M0}	methanol partial pressure in the feed
R	recirculation ratio
$\overline{R}$	ideal gas constant
Re	Reynolds dimensionless number
s_{BET}	BET specific surface
s_{micro}	microporous specific surface
S_i	carbon-based product i selectivity
S_h	other heat source items
S_m	mass source items
Sc	Schmidt dimensionless number
Sh	Sherwood dimensionless number
t	time
T	temperature
v	velocity
W	catalyst weight
X	carbon-based fractional conversion of oxygenates
y_i, y_{i0}, y_{is}	mole fraction of component i at certain condition, at the inlet, and at the catalyst surface, respectively
Y_i	carbon-based product i yield

Symbols

$\Delta y/y$	relative decrease on the mole fraction of reactants
θ	normalized time
μ	viscosity
υ_{total}	catalyst specific total volume
υ_{micro}	catalyst specific microporous volume
ρ	density
σ_θ^2	normalized variance
τ	viscous stress

Abbreviations

CSTR	continuous-stirred tank reactor
FTIR	Fourier-transform infrared
MS	mass spectrometry
MTH	methanol to hydrocarbons
MTO	methanol to olefins
PFR	plug flow reactor
RTD	residence time distribution
UV–vis	ultraviolet–visible

and consumables at affordable prices, making them attractive to the majority of the consumers [34,40]. Other researchers have decided to reinvent or redesign the cells for their purposes, making spinoff companies or amendments.

Meunier et al. [32] investigated commercial spectroscopic cells in detail, indicating that they are typically nonideal reactors (some commercial cells are flawed as kinetic reactors) and highlighted how some modifications improved their behavior as operando cell reactors for a better approach. The flaws concern the control of the catalyst bed temperature and bypass (related to large dead volumes and the probability of contact between the reactant molecules and catalyst). The fluid dynamics relevant to the vessel geometry, configuration, and fluid properties determine the proper measurement and analysis of the kinetic data [41–48]. Thus, Thomas et al. [42] conducted fluid dynamic simulations of an operando FTIR cell reactor using ANSYS Fluent to detect the flow nonidealities during methanol adsorption onto ceria due to the complex shape of the sample holder. This method was adequate for a better understanding of the fluid dynamic behaviors in the reactor and allowed kinetic investigations from the qualitative to fully quantitative aspects. Patil et al. [48] studied the fluid dynamics of a new diffuse reflectance cell using residence time distribution analyses, pulse experiments, and computational fluid dynamics modeling, which manifested a hybrid behavior of both laminar flow and continuously stirred tank reactors (CSTRs).

Most in situ or operando reaction studies of the MTH reaction have been carried out in commercial gas–solid spectroscopic cells, with little attention to assessing the behavior of these vessels as intrinsic kinetics reactors. Despite this, the analysis of the spectroscopic data from the in situ or operando reaction systems seems consistent with various conditions of catalysts or temperatures. The conclusions of these studies have verified that different catalysts with diverse morphology or acid properties and the reaction temperature variation modify the nature and formation kinetics of retained species in the MTH reaction [1,2,20,21,26–29,49]. However, one relevant experimental approach to obtain simultaneous kinetic and spectroscopic data is using an actual reactor with a UV–vis probe [1,27,49], which simultaneously analyzes the species formation on the catalyst surface and the species in the gas phase (kinetic data). This approach is satisfactory from a reaction engineering viewpoint, although it is limited to the use of UV–vis spectroscopy.

Our previous experience has demonstrated that two commercial gas–solid spectroscopic cells are suitable to study the formation kinetics of species on the catalyst surface during the MTH reaction with different catalysts [22,24,50] or cofeeding water [23,51] using FTIR or UV–vis spectroscopies. Accordingly, we verified that the formation rates of species decrease with a decreasing acid concentration in the catalyst and an increasing water concentration in the feed, which are the expected kinetic observations. We developed further an approach for analyzing the spectroscopic signatures with simultaneous online product analysis to correlate these with the reaction network in what is known as the spectro-kinetic methodology [52].

In this work, we conduct three analyses in each spectroscopic cell to properly analyze the kinetic data from these commercial gas–solid spectroscopic cells: fluid dynamics, comparison of the kinetics for the MTH reaction with a reference reactor, and assessment of mass transfer limitations. The fluid dynamics analysis is essential to determine the flow performance and model in the reaction vessel. The cell behavior as a flow reactor can be established, taking the plug flow reactor (PFR) or CSTR models as a reference. The fluid dynamic investigations validate the residence time distribution experimentally measured at room temperature, which allowed us to simulate the flow patterns at different spacetimes at the reaction conditions. We measured the kinetics of the

MTH reaction in each spectroscopic cell with variable spacetimes and compared the results with those obtained in a packed-bed reactor whose behavior is well known. Additionally, we discuss the implications of using a pressed disc of catalysts in these spectroscopic cells and the inherent potential internal mass transfer limitations when using thick discs (i.e., high catalyst loading) in this reaction. The novelty of this work relates to the development of a framework to assess the adequacy of these types of reactors where the results obtained will be more meaningful.

2. Methods

2.1. Catalyst preparation and characterization

An HZSM-5 zeolite-based catalyst was prepared by mixing 50 wt% of HZSM-5 zeolite with 30 wt% of pseudo-boehmite and 20 wt% of α-alumina, followed by drying at room temperature for 24 h and at 110 °C for 24 h more, crushing and sieving at 0.125 to 0.300 mm, and calcining at 550 °C for 3 h. The HZSM-5 is a commercial NH_4ZSM-5 (Zeolyst International, CBV8014, SiO_2/Al_2O_3 molar ratio = 80) calcined as described in a previous work [22] to obtain the acid form (HZSM-5). The catalyst was characterized using conventional techniques [22], including X-ray photoelectron spectroscopy (XPS), X-ray diffraction, N_2 physisorption, NH_3 adsorption, and temperature-programmed desorption (TPD), FTIR spectroscopy, and pyridine adsorption monitored with FTIR spectroscopy.

2.2. Packed-bed reactor

The MTH reaction was carried out in a conventional packed-bed reactor by varying the spacetime to obtain kinetic data using the following conditions: temperature (T) = 400 °C, total pressure (P) = 1.85 bar, methanol partial pressure (P_{M0}) = 1.57 bar, methanol molar fraction (y_{M0}) = 0.85, methanol flowrate (F_{M0}) = $1.00{\cdot}10^{-1}$ mol h^{-1}, total flowrate (F_0) = $1.18{\cdot}10^{-1}$ mol h^{-1}, catalyst weight (W) = 10 to 160 mg, methanol flowrate-based spacetime (W/F_{M0}) = 0.1 to 1.6 g h mol^{-1}, or total flowrate-based spacetime (W/F_0) = 0.085 to 1.360 g h mol^{-1}. The reaction setup is described in detail in a previous publication [22]. Briefly, the reactor is a stainless steel tube (inner diameter = 9 mm) with a packed-bed arrangement of 6 cm^3 consisting of a mixture of SiC (VWR Chemicals, < 0.105 mm) and catalyst sample (0.1 g), which is inside a hot box kept at 200 °C to prevent the condensation of the products for analysis in gas–vapor phase. The feed consisted of pure liquid methanol pumped at 0.1 mol h^{-1} and diluted with He. The product analysis was carried out online using a micro-gas chromatograph (GC) (Varian, CP4900) with a thermal conductivity detector and three column channels for simultaneous analysis: 1) Molesieve 5A (fumed SiO_2, packed length = 8 m, column temperature = 45 °C, column injection temperature = 65 °C, and column pressure = 1.8 bar) for separating N_2, O_2, CO, and CH_4; 2) PoraPLOT Q (packed length = 10 m, column temperature = 80 °C, column injection temperature = 80 °C, and column pressure = 1.8 bar) for separating C_1-C_4 hydrocarbons and oxygenates; and 3) CP-Sil 5 CB (packed length = 10 m, column temperature = 80 °C, column injection temperature = 80 °C, and column pressure = 1.8 bar) for separation of C_4-C_{10} hydrocarbons and oxygenates. The conversion (X) is calculated assuming that all identified oxygenates (methanol and dimethyl ether) are reactants on a carbon-mole basis:

$$X = \frac{F_{M0} - F_M}{F_{M0}} = 1 - Y_M \tag{1}$$

where F_{M0} is the carbon-based molar flowrate of oxygenates in the feed (inlet), F_M denotes the carbon-based molar flowrate of oxygenates in the outlet, and Y_M represents the carbon-based yield of oxygenates in the outlet. The carbon-based yield of a product i (Y_i) or the carbon-based selectivity of a product i (S_i) is calculated as follows:

$$Y_i = \frac{F_i}{F_{M0}} \tag{2}$$

$$S_i = \frac{F_i}{F_{M0} - F_M} = \frac{Y_i}{X} \tag{3}$$

where F_i indicates the carbon-based molar flowrate of product i.

2.3. Spectroscopic cell reactors

Two commercial spectroscopic cells were used as reactors:

(i) Specac cell reactor: a Specac HTHP (high-pressure high-temperature) cell with applications in transmission FTIR spectroscopy, used in a Thermo Scientific, Nicolet 6700, FTIR spectrometer.
(ii) Linkam cell reactor: a Linkam THMS600 stage/cell with applications in FTIR, UV–vis, Raman spectroscopies and other microscopies, used in a Jasco V-780, UV–vis spectrometer with a specially adapted compartment (Jasco, ARN-915i) for the cell.

For either cell, the catalyst was loaded in the form of a pressed disc obtained by pressing a sample of catalyst powder at 10 t of pressure in a Specac manual hydraulic press.

Fig. 1 illustrates a schematic representation of the inner geometry of the Specac cell reactor (refer to the manufacturer for further details). This cell is configured to work in transmission mode, requiring a thin sample placed vertically and aligned between two windows (one of the windows is at the back according to this representation, so it is not seen in this drawing). Thus, the inner geometry of the Specac cell reactor consists of a rectangular parallelepiped vessel with an irregular polyhedron solid heating element inside. The heating element stands on one of the vessel lateral lids and has a cylindrical hole for placing and holding the catalyst disc. Thus, the void volume where the flow passes through is the vessel volume minus the heating element volume, resulting in a complex geometry for the flow volume. The void/flow volume is larger than the catalyst volume, and therefore the probability of contact between the catalyst and molecules in the fluid phase may be low.

Fig. 2 shows the inner geometry of the Linkam cell reactor (refer to the manufacturer for further details). This cell was configured to work in diffuse reflectance mode using an integrating sphere placed on the cell window, requiring that the sample is placed horizontally, and aligned with the window. The vessel geometry is complex, consisting of a cylindrical volume with two additional parallelepiped volumes (dead volumes) hosting other elements for the cell functioning. The heating element (stage) is a smaller cylinder on the vessel ground face, and the sample disc is on the top face. Thus, the void/flow volume is approximately the vessel volume minus the heating element volume, resulting in a complex geometry with possibly significant dead volumes. Likewise, this configuration does not provide complete contact between the catalyst disc and flow, as it may also happen in the Specac cell reactor.

2.3.1. Kinetics in cell reactors

The MTH reaction was carried out in the spectroscopic cells varying the spacetime to obtain basic kinetic data and deactivation performance using the following conditions: T = 400 °C, P = 1 bar, P_{M0} = 0.05 or 0.16 bar, F_{M0} = $9.38{\cdot}10^{-4}$ to $6{\cdot}10^{-2}$ mol h^{-1}, F_0 = $1.88{\cdot}10^{-2}$ to $3.75{\cdot}10^{-1}$ mol h^{-1} or 7 to 140 mL min^{-1} at standard temperature and pressure, W = 12 or 48 mg, W/F_{M0} = 0.2 to 12.8 g h mol^{-1} or W/F_0 = $3.20{\cdot}10^{-2}$ to $6.40{\cdot}10^{-1}$ g h mol^{-1}. Fig. 3 presents the general experimental setup for both spectroscopic cells, which was the same. Accordingly, the feed consisted of N_2 with methanol vapor obtained by flowing N_2 through a vessel containing liquid methanol (saturator) at room temperature or by immersing it in an ice bath. The methanol concentration was calculated

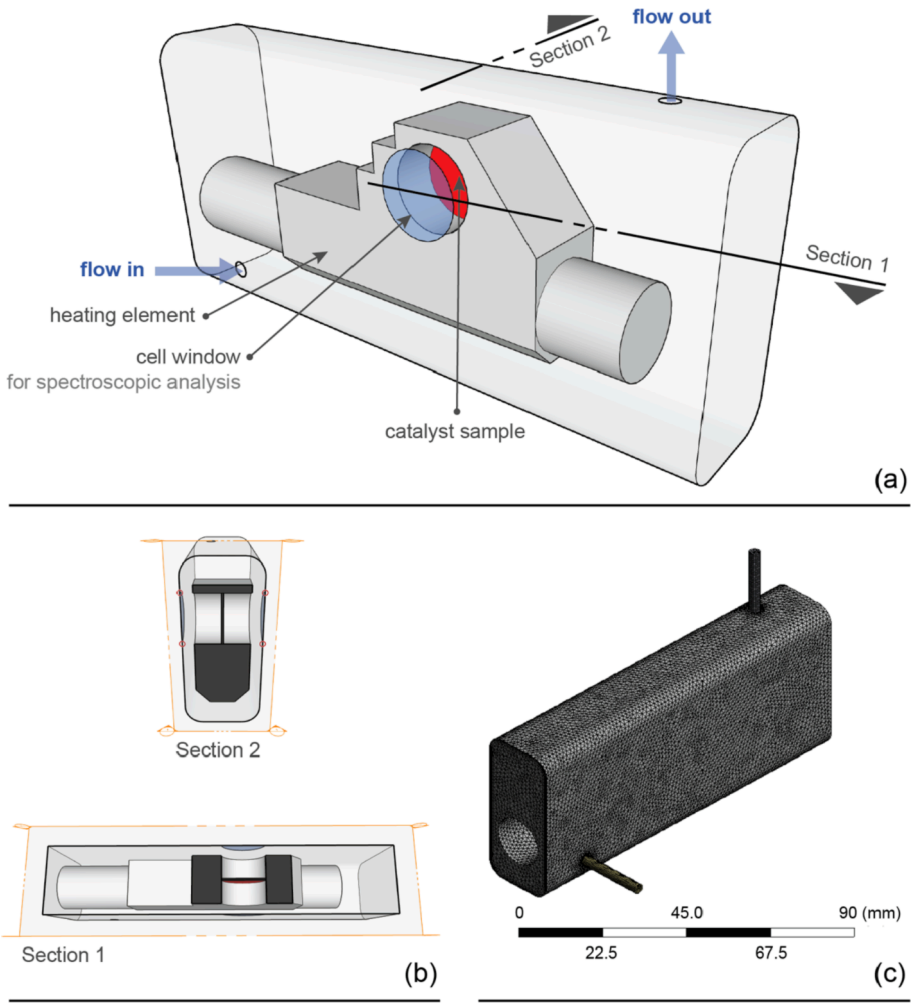

Fig. 1. Schematic representation of the commercial Specac cell designed for working with Fourier-transform infrared spectroscopy: (a) perspective view, (b) section cuts, and (c) mesh model.

using the equilibrium data at room temperature or 2 °C (temperature measured in the liquid methanol when the vessel was immersed in an ice bath). The equilibrium calculations indicated that the methanol molar fraction in the feed (y_{M0}) was 0.16 at 25 °C and 0.05 when the methanol was immersed in an ice bath. The products in the gaseous outlet were analyzed using a mass spectrometer (MS; Pfeiffer Vacuum, OmniStar GSD 320O Series), which continuously measured the m/z signals of 16, 18, 27, 29, 31, 41, 43, 45, 55, 56, 57, 78, and 91. Additionally, the gaseous outlet is analyzed for two experiments by sampling every 20 min and measuring the gas composition in the micro-GC (Varian, CP4900) previously described in order to correlate both analyses of the gaseous outlet and to calculate the conversion of oxygenates and yield of the product lumps.

Additional experiments were carried out to evaluate the possible internal mass transfer limitations in the Linkam cell reactor. These experiments consisted of using different catalyst weights (W = 12 to 48 mg) and flowrates (F_{M0} = 1.88 to 7.50·10^{-3} mol h^{-1} or F_0 = 3.75·10^{-2} to 1.50·10^{-1} mol h^{-1}) to obtain the same spacetime (W/F_{M0} = 6.4 g h mol^{-1} or W/F_0 = 0.32 g h mol^{-1}). The spent catalyst in the experiment with the highest catalyst weight was further studied using scanning electron microscopy (SEM) and energy-dispersive X-ray spectroscopy (EDX). The spent catalyst disc was cut perpendicularly and coated with gold. Various SEM images were taken at the disc surface and cut section with an elemental analysis using EDS in a JEOL JSM-7000F microscope with a tungsten filament (resolution 3.5 nm) equipped with an Oxford Pentafet EDS analyzer (resolution 133 eV) operating at 20 kV under a vacuum of 9.65·10^{-5} bar and an intensity of 1.85·10^{-10} A. Likewise, the capacity of N_2 adsorption–desorption in the catalyst powder and pressed catalyst sample was studied using a Micromeritics ASAP 2010 apparatus. The experimental procedure consisted of outgassing the sample at 150 °C and 10^{-3} mmHg for 8 h, followed by N_2 adsorption and desorption at –196 °C to obtain isothermal equilibrium data to calculate the specific surface area and volume using the Brunauer-Emmett-Teller (BET) method.

2.3.2. *Residence time distribution*

The fluid dynamic performance of spectroscopic cells was assessed by carrying out residence time distribution measurements based on a step tracer signal stimulus–response technique using the experimental setup in Fig. 3. The measurements were carried out at variable flowrates using methanol as a tracer, without a catalyst in the following conditions: T = 25 °C, P = 1 bar, P_{M0} = 0.05 or 0.16 bar, F_{M0} = 9.38·10^{-4} to 6·10^{-2} mol h^{-1}, F_0 = 1.88·10^{-2} to 3.75·10^{-1} mol h^{-1}, or 7 to 140 mL min^{-1} at standard temperature and pressure. The procedure consists of two independent N_2 flowrates, one of which passes through a methanol saturator. These two streams are the inlet to a set of valves, and the outlets move to the spectroscopic cell or vent. Initially, the pure N_2 flow passes through the spectroscopic cell, whereas the one that passes through the methanol saturator is vented until stabilized. Upon stabilization, the feed is switched to the stream saturated in methanol. The time is set to zero, and the outlet from the spectroscopic cell is continuously analyzed using the MS. The MS signal associated with methanol

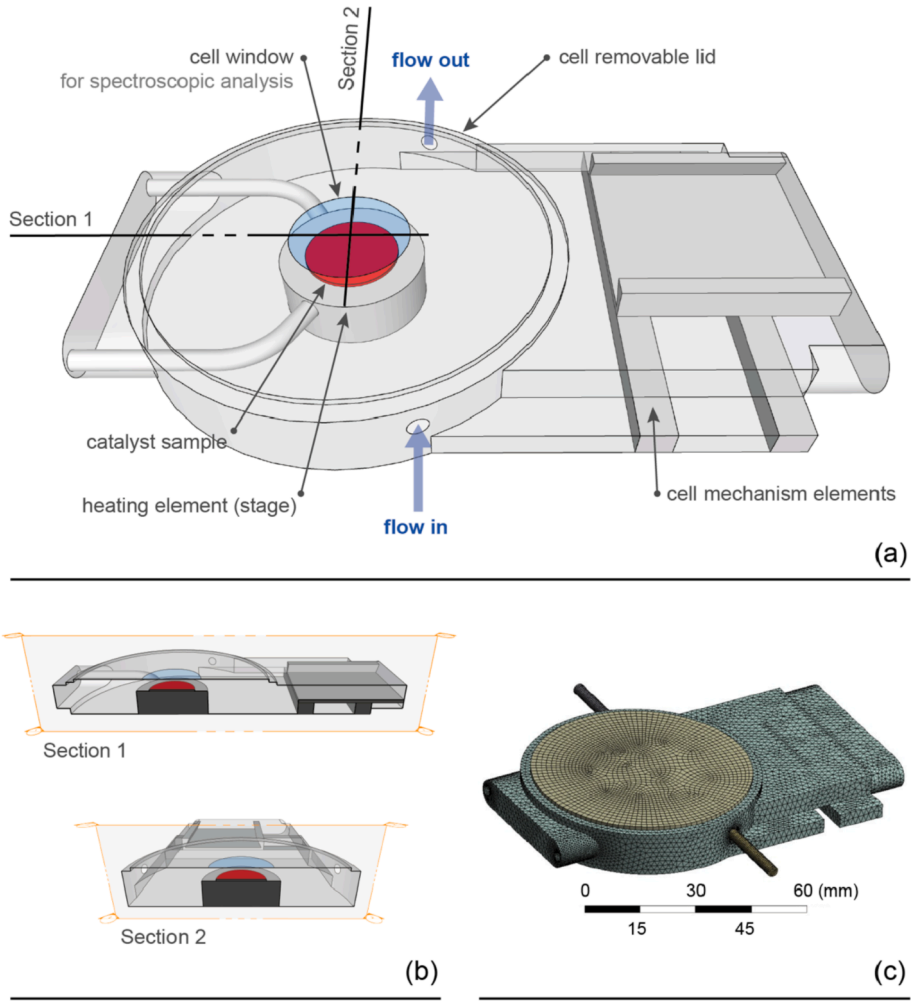

Fig. 2. Schematic representation of the commercial Linkam cell designed for working with ultraviolet–visible spectroscopy and other microscopic applications: (a) perspective view, (b) section cuts, and (c) mesh model.

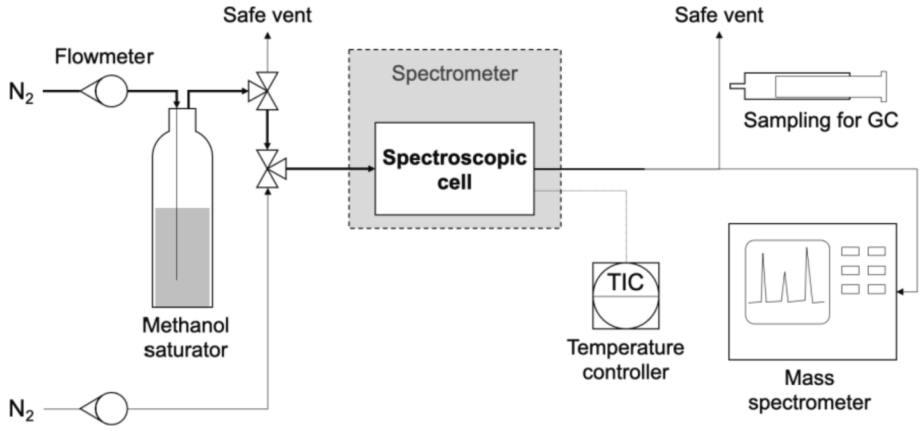

Fig. 3. Process flow diagram of the experimental setup for the use of spectroscopic cells as reactors.

($m/z = 31$) is analyzed to obtain the residence time distribution profiles.

The concentration–time curve at the cell outlet, measuring the inlet tracer concentration ($c(t)/c_0$) and normalized time ($\theta = t/\tau$) by dividing it by the mean residence time ($\tau = V/Q$), is the normalized cumulative distribution function or $F(\theta)$ curve [53] that is differentiated to obtain the fractional distribution function or $E(\theta)$ in Eq. (4). The mean residence time and variance are calculated using the same equations described in classical reaction engineering books [53,54]. This information is helpful to determine the characteristics of the flow in a nonideal reactor either by relating it to a dispersion model or several (ideal) CSTRs in series. The latter assumes that the actual reactor is represented by a series of N equal-size well-mixed tanks with a total volume equal to that of the analyzed reactor. For a system in which the inlet and measurement are carried out away from the analyzed cell

(closed system), the number of equivalent CSTRs connected in series is determined as [53]:

$$N = \frac{1}{\sigma_\theta^2} \tag{4}$$

The experimental residence time distribution function and number of equivalent tanks connected in series can be compared to theoretical values. Hence, the $E(\theta)$ curve for a given number N of tanks is obtained by the following [53]:

$$E(\theta)_{theoretical} = \frac{N^N \theta^{N-1}}{(N-1)!} e^{-N\theta} \tag{5}$$

2.4. Fluid dynamic simulations of cell reactors

Nonreactive steady- and transient-state simulations inside the two spectroscopic cells were performed in ANSYS Fluent [55] to obtain the three-dimensional flow fluid dynamics in the conditions used in the experiments described in Section 2.3. The modeling strategy consisted of simulating the residence time distribution and obtaining the flow pattern predictions in the reaction conditions. Considering the low Reynolds number inside the domain, a laminar flow was assumed. With the species transport model, the gas concentration distributions can be monitored. A gravitational acceleration of -9.81 m s^{-2} was assigned for each cell, the direction of which was determined by the geometry. The no-slip boundary was chosen for all walls. The semi-implicit method for pressure linked equations-consistent (SIMPLEC) algorithm was applied for the coupling of velocity and pressure, and the second-order upwind scheme was used for the momentum, energy, and species transport equations. The absolute convergence criterion of 10^{-3} was set for all equations except for energy by 10^{-6}.

2.4.1. Computational fluid dynamics model

The conservation equations [55] of mass, momentum, and energy are as follows:

$$\frac{\partial \rho}{\partial t} + \nabla \bullet (\rho \vec{v}) = S_m \tag{6}$$

where ρ is the density, v denotes the velocity, t represents time, S_m indicates the other mass source items, and the operator ∇, referred to as "grad" represents the partial derivative of a quantity concerning all directions in the chosen coordinate system. Further,

$$\frac{\partial}{\partial t}(\rho \vec{v}) + \nabla \bullet (\rho \vec{v} \vec{v}) = -\nabla p + \nabla \bullet (\bar{\bar{\tau}}) + \rho \vec{g} + \vec{F} \tag{7}$$

where p is the pressure, $\bar{\bar{\tau}}$ represents the stress tensor, and $\rho \vec{g}$ and $\vec{F}$ denote the gravitational body force and external body forces. Finally,

$$\frac{\partial}{\partial t}(\rho E) + \nabla \bullet [\vec{v}(\rho E + p)] = \nabla \bullet \left[k_{\text{eff}} \nabla T - \sum_j h_j \vec{J}_j + (\overline{\overline{\tau_{\text{eff}}}} \bullet \vec{v}) \right] + S_h \tag{8}$$

where E denotes the total energy of the fluid, h indicates the enthalpy, τ denotes the viscous stress, and S_h represents the other heat source items. Moreover, J_j represents the diffusion flux, the expression of which is presented in Eq. (9) in laminar flow:

$$\vec{J_i} = -\rho D_{i,m} \nabla Y_i - D_{T,i} \frac{\nabla T}{T} \tag{9}$$

where $D_{i,m}$ is the mass diffusion coefficient for species i in the mixture, and $D_{T,i}$ is the thermal diffusion coefficient.

2.4.2. Mesh model

Further, ANSYS Workbench [56] was adopted to generate the mesh models of spectroscopic cells by adjusting the element size. The catalyst disc is considered as a wall boundary through which the fluid cannot flow because it was obtained by pressing a sample of catalyst powder at 10 t of pressure. Based on this, steady-state simulations under selected conditions ($T = 25$ °C, $P = 1$ bar, $P_{M0} = 0.16$ bar, and $F_{M0} = 0.06$ mol h^{-1}) were carried out to perform a mesh independence check. The inlet velocity was calculated from the feed flowrate, whereas the outlet pressure was set to zero with other settings at default. By comparing the inlet pressure with different mesh models of each cell, the mesh model with the mesh size of 373,049 for the Specac cell reactor in Fig. 1c and the mesh model with the mesh size of 259,410 for the Linkam cell reactor in Fig. 2c display velocity distribution results similar to the models with larger mesh sizes. Moreover, fewer computation efforts were needed. Thus, these two mesh models were selected for further simulations considering the calculation efficiency and precision.

2.4.3. Simulation procedures

The residence time distribution inside the cell was obtained using the step injection technique of the tracer [53] with the same conditions in Section 2.3.2 using the velocity-inlet and pressure-outlet boundary conditions to validate the computational fluid dynamics approach. Starting from the converged steady-state simulation of pure N_2 flow, the mixture of N_2 and methanol was injected into the cell for transient-state simulation at time $t = 0$ s. The monitor point at the exact location as in the experiments was reported in a continuous mode for the methanol concentration curve with the flow time, from which the residence time distribution was calculated.

The flow patterns under the reaction conditions (Section 2.3.1) can be predicted with the verified simulation strategy during the reaction conditions. Due to the unneglectable temperature gradient in the cells, the temperature-dependent physical parameters of methanol and nitrogen (Table S1) were fitted and compiled into the materials of ANSYS Fluent. The cell surfaces were treated as walls with a constant temperature due to the highly efficient heat transfer of the metallic cells. In this way, the velocity-inlet and pressure-outlet boundary conditions were adopted to study the flow fluid dynamics in the reaction conditions (as in Section 2.3.1) of $P_{M0} = 0.16$ bar for both the Specac and Linkam cell reactors with other settings at the default.

3. Results

3.1. Fluid dynamic performance

The fluid dynamics of spectroscopic cells were evaluated using experimental and computational methods. Accordingly, the residence time distribution was measured experimentally and verified using fluid dynamic simulations. Additionally, the dynamic simulations provided flow patterns inside the spectroscopic cells.

3.1.1. Residence time distribution

Fig. 4 presents the experimental and simulated residence time distribution curves, $E(\theta)$, for the Specac cell reactor in Fig. 4a and Linkam cell reactors in Fig. 4b, and the corresponding theoretical residence time distribution representations for ideal CSTR and PFR systems (Eq. (5)).

The performance of both spectroscopic cells is in between the ideal CSTR and PFR systems and slightly varies according to the flowrate (more markedly for the Specac cell reactor). Additional theoretical residence time distribution representations for a different number of tanks (N) indicate that the deviation from the ideal CSTR and PFR systems can approach a certain number of CSTR in series. Thus, the Specac cell reactor is between two and four tanks in series, and the Linkam cell reactor is between one and three in series. At very low flowrates, the increasing importance of the dead volume zones generates a deviation of the flow by developing a long tail in the Linkam cell reactor. Except for that flow, although not ideal, the cell behavior is similar at different flowrates when time is normalized. The residence time distribution curves of the Specac cell reactor also deviate from the ideal case due to bypass or plug flow patterns between the cell inlet and outlet.

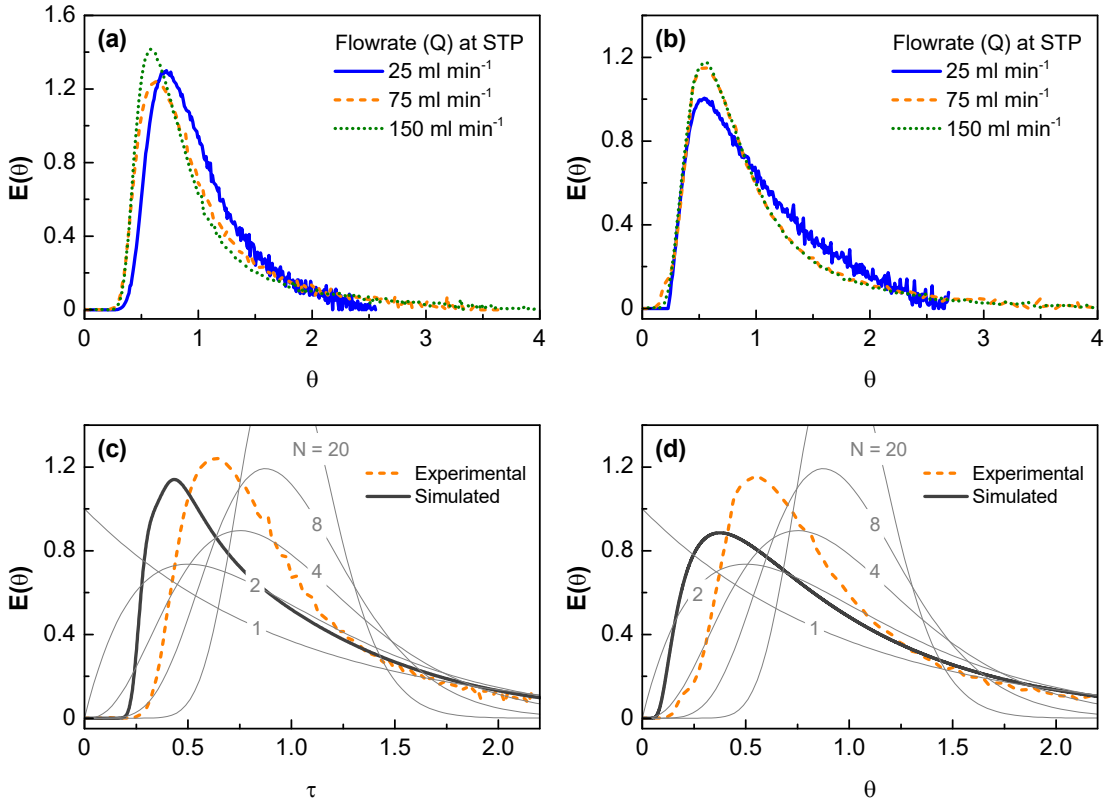

Fig. 4. Experimental residence time distribution profiles at different flowrates for (a) Specac and (b) Linkam cell reactors and the comparison of the experimental, simulated and theoretical residence time distribution profiles for *N* tanks in series for the (c) Specac and (d) Linkam cell reactors. STP stands for standard temperature (0 °C) and pressure (1 bar) conditions.

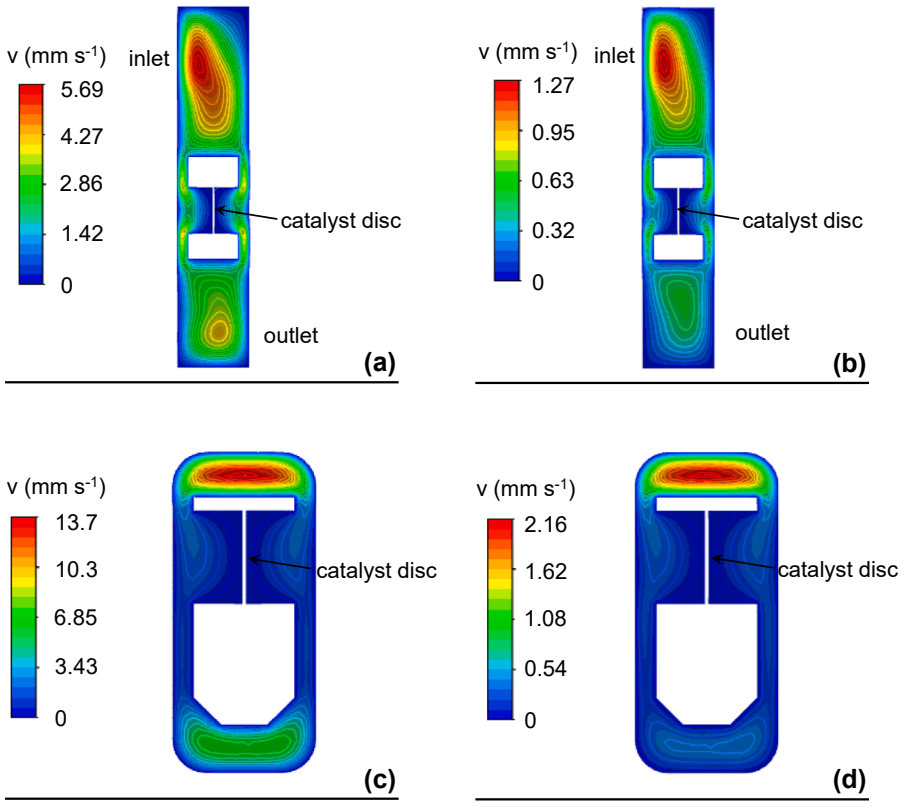

Fig. 5. Simulated gas velocities in steady-state conditions for the Specac cell reactor: velocity profile for Section 1 at flowrates of (a) 0.06 mol h^{-1} and (b) 0.0075 mol h^{-1} and for Section 2 at flowrates of (a) 0.06 mol h^{-1} and (b) $7.5{\cdot}10^{-3}$ mol h^{-1}. Simulation conditions: $T = 400$ °C, $P = 1$ bar, $P_{M0} = 0.16$ bar.

The comparison between experimental and calculated $E(\theta)$ curves is relatively satisfactory but not ideal. The discrepancies, especially regarding the maximum value of the function $E(\theta)$, highlight the intricate internals of these cell reactors, which are designed for multiple objectives including the acquisition of meaningful spectroscopic information. The existence of connections, stagnant and dead volume zones plus other non-idealities is responsible for these deviations.

3.1.2. Simulated flow patterns

Upon validation of the flow model, we simulated the flow patterns in spectroscopic cells at the reaction conditions. Fig. 5 illustrates the simulated velocities for the representative planes of the Specac cell reactor (Fig. 1b) under various flowrates, and Figure S1 shows the corresponding flow paths. The simulations at different flowrates indicate that the velocity and, consequently, the Reynolds number decrease with decreasing flowrates, as expected. Dead volume zones appear near the inlet and outlet of the reactor vessel, which have almost zero velocity at the corner. Similar velocity distributions are observed for different flowrates, with a gradual decrease from the inlet to the catalyst disc surface, where another dead volume zone appears. The calculated Reynolds numbers vary at different cell locations in the same way as the velocities, and the values are almost at the magnitude of 10^{-2} due to the low flowrate at the inlet. In this regard, the flow momentum is transported by viscous diffusion not by convection, so eddies appear upstream and downstream of the heating element of the Specac cell reactor. The above phenomenon leads to fluid dynamics with mixing from the upstream and the catalyst disc surface and several dead volume zones in the cell. Hence, it resembles a nonideal CSTR. As depicted in Figs. 5c-d, part of the gas flows horizontally from the bottom side of the cell with a relatively high velocity without touching the catalyst disc. The fluid fraction that bypasses the catalyst through the bottom of the cell decreases with the flowrate decline, leading to better gas–solid contact. Moreover, a lower flowrate implies a longer residence time inside the cell. Hence, the conversion is expected to increase due to the improved flow pattern and increased contact time.

Fig. 6 presents the simulated velocities for the representative sections in Fig. 2b of the Linkam cell reactor at various flowrates, and Figure S2 shows the corresponding flow paths. The simulation results confirm that the velocity decreases with the decline in the flowrate, as expected. Similar velocity distributions are observed for the highest and lowest flowrates, with a gradual decline from the inlet to the catalyst disc surface toward the outlet. Although two local flow eddies appear near the inlet, the small velocity gradient above the catalyst site surface indicates a well-mixed area even without a stirring element in the cell. In contrast, dead volume zones are observed near the outlet with a relatively large zero-velocity area. The Reynolds number ranges from 10^{-2} to 10^{-1}, manifesting a slow flow, but the flow velocity of the gas phase is higher than that in the Specac cell reactor. However, dead volume zones with almost zero velocity at the upside and downside corners of the cell are apparent. The mentioned phenomenon indicates the fluid dynamics of mixing from the upstream and catalyst disc surface and reveals several dead volume zones in the cell, far from the behavior of an ideal reactor.

Comparing the simulated fluid dynamics, the velocities above the catalyst disc (where the reaction occurs) of the Specac cell reactor are relatively low, almost like dead volume zones. In contrast, an effective

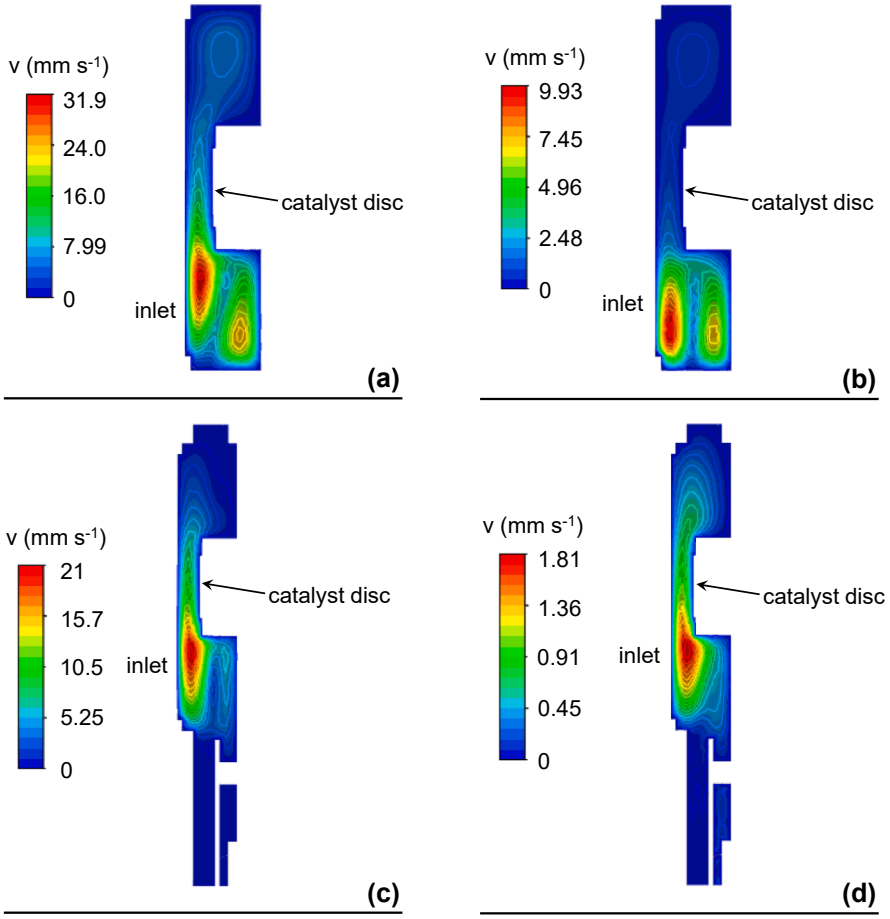

Fig. 6. Simulated velocities in steady-state conditions for the Linkam cell reactor: velocity profile for Section 1 at flowrates of (a) $6.0{\cdot}10^{-2}$ mol h^{-1} and (b) $7.5{\cdot}10^{-3}$ mol h^{-1} and for Section 2 at flowrates of (a) $6.0{\cdot}10^{-2}$ mol h^{-1} and (b) $7.5{\cdot}10^{-3}$ mol h^{-1}. Simulation conditions: $T = 400$ °C, $P = 1$ bar, $P_{M0} = 0.16$ bar.

fluid flow occurs above the catalyst disc for the Linkam cell reactor with relatively high velocity in small gradients. The Specac cell reactor resembles a CSTR because of the stagnant flow, whereas the reason for the resemblance is the back-mixing for the Linkam cell reactor. These results agree with those obtained in the experimental residence time distribution curves. Thus, based on the characteristic back-mixing phenomenon of CSTR systems, the behavior of the Linkam cell reactor resembles that of CSTR (although not ideal) more than the Specac cell reactor. The deviation from the ideality of the Linkam cell reactor as a CSTR system is due to its large dead and stagnant volumes as well as the velocity gradient.

3.2. Kinetic performance

The components in the gas phase using MS or GC analyses in the three reaction systems (packed-bed, Specac and Linkam cell reactors) are oxygenates (methanol and dimethyl ether) and typical hydrocarbon products of the MTH reaction. Fig. 7 presents the product distribution profiles regarding the yield against conversion for the three reaction systems, in which the hydrocarbon products were grouped as light olefins (LO), the sum of light paraffins and heavy aliphatics (LP + HA), and aromatics (BTX). Product yields rise with increasing conversions, and the product distribution profiles are similar and almost overlapping

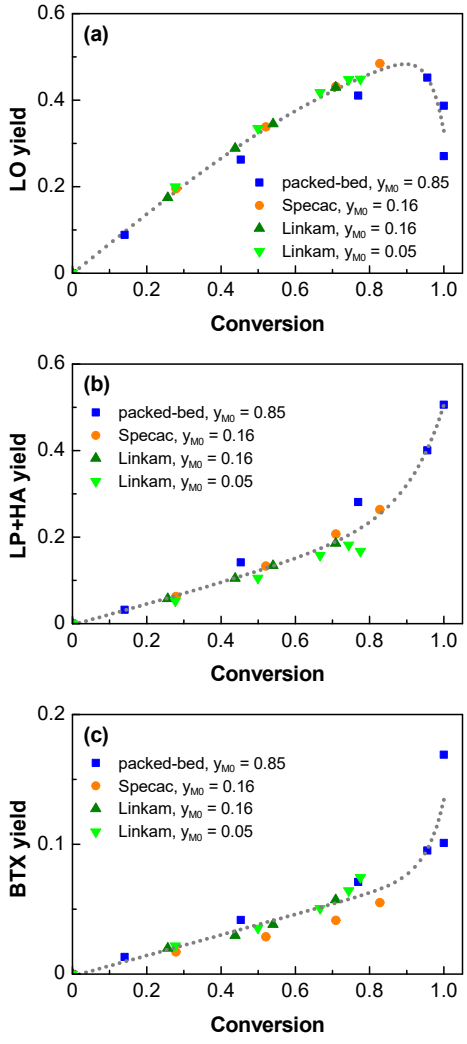

Fig. 7. Product distribution profiles for the three reaction systems: (a) light olefin (LO), (b) sum of light paraffins and heavy aliphatics (LP + HA), and (c) aromatics (BTX).

for the three reaction systems. However, the experimental data of the packed-bed reactor further reveals that the light olefins yield (Fig. 7a) decreases at high conversions (reaching a maximum), an expected result for the MTH reaction, as light olefins are typically intermediates in the kinetic scheme [16,57–59]. Likewise, the apparent continuous increase in the yields of heavy aliphatics, light paraffins and aromatics at high conversions indicates that these are the final products of the reaction scheme. These products are formed from the oligomerization/methylation of light olefins, yielding heavy aliphatics, and hydrogen transfer reactions producing light paraffins and aromatics.

Fig. 8 presents the conversion profiles against spacetime defined as the ratio between the catalyst weight (W) and total molar flowrate (F_0) for experiments carried out in the three reaction systems. The experimental data (Fig. 8a) indicate that the conversion increases with increasing spacetime, which grows much faster in spectroscopic cells than in the packed-bed reactor. The conversion profile of the packed-bed reactor describes an autocatalytic reaction that can be modeled with a simple kinetic scheme, as demonstrated by Janssens et al. [60,61] and in our previous studies [23,50], as follows:

$$M \xrightarrow{k_1} H \tag{10}$$

$$M + H \xrightarrow{k_2} H + H \tag{11}$$

where M denotes oxygenates and H represents all hydrocarbon products (olefin, paraffin, and aromatics) formed in the MTH reaction. Thus, the reaction rate of oxygenates is written as follows:

$$-r_M = k_1 y_M + k_2 y_M y_H \tag{12}$$

where y_M and y_H are the molar fractions of oxygenates and hydrocarbons in the reaction medium, respectively; therefore, $y_{M0} = y_M + y_H$, where y_{M0} is the molar fraction of oxygenates (methanol) in the feed. Based on the conversion of oxygenates (X), $y_M = y_{M0}(1 - X)$ and $y_H = y_{M0}X$, so that the reaction rate of oxygenates becomes the following:

$$-r_M = y_{M0}(1 - X)(k_1 + k_2 y_{M0} X) \tag{13}$$

This kinetic expression is used to solve the design equation of a PFR system, which theoretically describes the behavior of the packed-bed reactor:

$$\frac{W}{F_{M0}} = \frac{W}{F_0 y_{M0}} = \int_0^X \frac{dX}{y_{M0}(1 - X)(k_1 + k_2 y_{M0} X)} \tag{14}$$

where F_{M0} is the molar flowrate of oxygenates (methanol) in the feed. After integrating and reordering, we obtain.

$$X = \frac{k_1\left(e^{\frac{W}{F_0}(k_1 + k_2 y_{M0})} - 1\right)}{k_2 y_{M0} + k_1\left(e^{\frac{W}{F_0}(k_1 + k_2 y_{M0})}\right)} \tag{15}$$

Eq. (15) fits the experimental data of the packed-bed reactor (dashed line in Fig. 8a), confirming the autocatalytic nature of the MTH reaction in this reaction system. The kinetic coefficients are $k_1 = 8.51 \cdot 10^{-1}$ mol (g h)$^{-1}$ and $k_2 = 18.6$ mol (g h)$^{-1}$, indicating that the initial formation of hydrocarbons (k_1) is the slower step (induction) in which active surface species are formed. In other words, this conversion profile indicates a critical spacetime is required for the sufficient formation of surface species. However, the conversion profiles of the spectroscopic cells do not describe autocatalytic kinetics because the conversion rapidly increases at low spacetimes, apparently suppressing the induction step (a slow increase in the conversion at low spacetimes observed in the packed-bed reactor, in which hydrocarbons are slowly formed). Instead, the experimental conversion profiles of the spectroscopic cells seem to resemble first-order kinetics.

However, from the fluid dynamic analysis, the behavior of the spectroscopic cells is close to a CSTR system. In theory, the CSTR system is more adequate for autocatalytic reactions at low conversions (low spacetimes) [53] than a PFR one, which was demonstrated by Müller

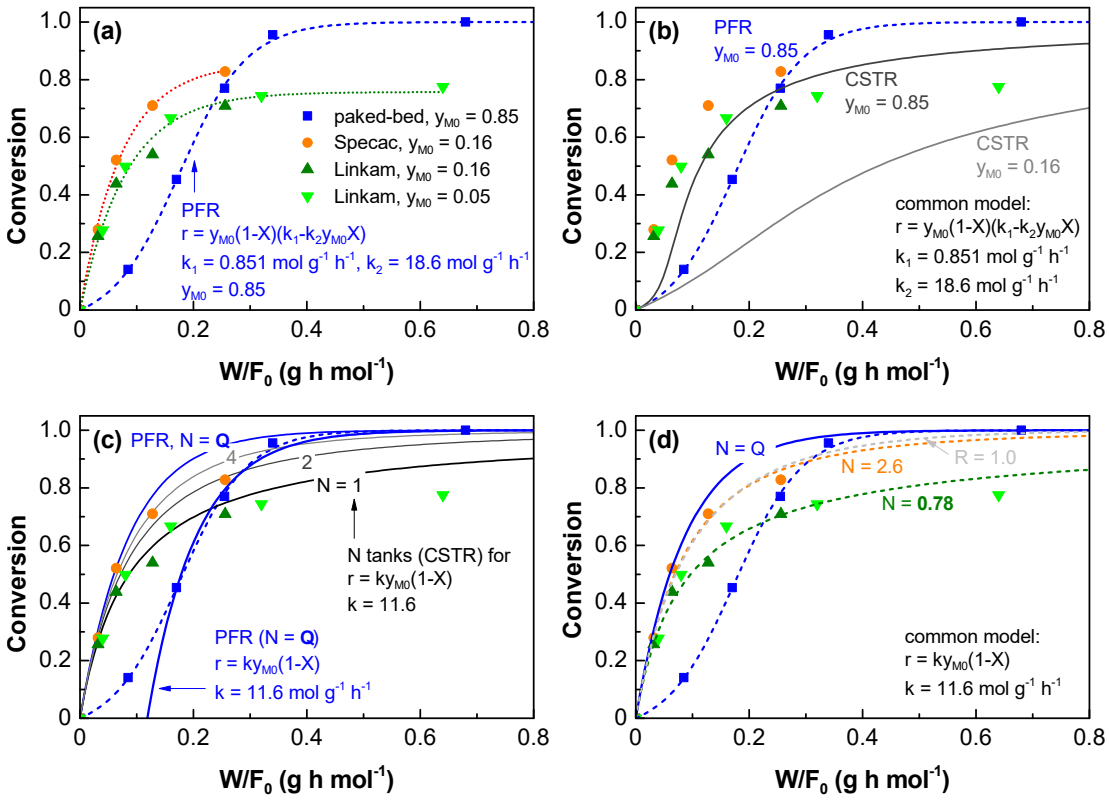

Fig. 8. Conversion profiles for the Specac and Linkam cell and packed-bed reactors for the methanol-to-hydrocarbon (MTH) reaction at 400 °C: (a) experimental data, (b) comparison with an autocatalytic kinetic model, (c) comparison with a first-order kinetic model, and (d) fitting to a first-order kinetic model for *N* tanks (continuously stirred tank reactors, CSTRs) in series.

et al. [59] for the MTH reaction. This finding verified the rapid increase in the conversion at short contact times in a CSTR system in contrast with a PFR system. This outcome was attributable to the homogeneous distribution of products in the back-mixed reactor (CSTR system), leading to a rapid accumulation of active surface species, enabling the fast reaction pathways. Thus, we simulated the autocatalytic kinetics of the MTH reaction in a CSTR system:

$$\frac{W}{F_{M0}} = \frac{W}{F_0 y_{M0}} = \frac{X}{y_{M0}(1-X)(k_1 + k_2 y_{M0} X)} \tag{16}$$

Reordering and solving for X,we obtain the following:

$$X = \frac{\sqrt{k_1{}^2\left(\frac{W}{F_0}\right)^2 + 2k_1\frac{W}{F_0}\left(k_2 y_{M0}\frac{W}{F_0}+1\right) + \left(k_2 y_{M0}\frac{W}{F_0}-1\right)^2} - k_1\frac{W}{F_0} + k_2 y_{M0}\frac{W}{F_0} - 1}{2k_2 y_{M0}\frac{W}{F_0}} \tag{17}$$

Eq. (17) models the autocatalytic kinetics of the MTH reaction in a CSTR system using the parameters k_1 and k_2 fitted from the packed-bed reactor experimental data. This model depends on the initial molar fraction of oxygenates (y_{M0}); therefore, we plotted a curve for $y_{M0} = 0.85$ (used in the packed-bed reactor) and $y_{M0} = 0.16$ (in spectroscopic cells) as depicted in Fig. 8b. The experimental data for the spectroscopic cells are around the curve of $y_{M0} = 0.85$, whereas they are far above the curve for $y_{M0} = 0.16$. If the experimental data had corresponded to an autocatalytic model, it would have been expected that the conversion profiles for the spectroscopic cells would have been around the curve for $y_{M0} = 0.16$. Thus, we ruled out that the experimental data for the spectroscopic cells follow an autocatalytic kinetic model. Instead, the conversion profiles of spectroscopic cells resemble a first-order kinetics. The conversion profiles strengthen this hypothesis for two different overlapped initial molar fractions of oxygenates (0.16 and 0.05) in the Linkam cell reactor. Theoretically, the conversion profiles (conversion against W/F_0) of first-order kinetics do not depend on the initial molar fraction of the reactant [53].

The conversion profile of the packed-bed reactor was converted into a first-order kinetic model following the approach reported by Janssens et al. [60] to compare the experimental conversion profiles for the spectroscopic cells with those for the packed-bed reactor. Accordingly, the experimental data of the packed-bed reactor were fitted to first-order kinetics in a PFR system for conversions above 0.4 (when the induction step is overcome, and the reaction rate rapidly increases), as follows:

$$X = 1 - e^{-k\left(\frac{W}{F_0} - \left(\frac{W}{F_0}\right)_{crit}\right)} \tag{18}$$

where k is the first-order kinetic coefficient and $(W/F_0)_{crit}$ is the critical spacetime at which the induction step is overcome (definition provided in [60]). Fitting the experimental data of the packed-bed reactor to Eq. (18) results in k = 11.6 mol (g h)$^{-1}$ and $(W/F_0)_{crit} = 1.19{\cdot}10^{-1}$ g h mol^{-1} (Fig. 8c). With the parameters from this fitting, theoretical curves were plotted considering $(W/F_0)_{crit} = 0$ (i.e., theoretically suppressing the induction step for the conversion profile of the packed-bed reactor) for a PFR system (N →∞) and CSTR system with one tank ($N = 1$) or a variable number of tanks (N tanks in series of the same size). The fitting expression is deduced from solving the CSTR design equation for the first-order kinetics for N tanks in series [53]:

$$X = 1 - \frac{1}{\left(1 + 11.6\frac{W/F_0}{N}\right)^N} \tag{19}$$

Fig. 8c reveals that the conversion profile of the Specac cell reactor approaches a theoretical curve for two or four tanks (CSTR) in series, whereas that of the Linkam cell reactor is close to one CSTR. Assuming the ideal kinetic control (in absence of another effect), we fitted the experimental conversion profiles of the spectroscopic cells to Eq. (19) to

determine the actual number of tanks (N) that satisfactorily describes the experimental data. Fig. 8d shows the fitting results, indicating that the conversion profile of the Specac cell reactor is well described by the first-order kinetics for 2.6 tanks (CSTRs) in series, whereas that of the Linkam cell reactor is successfully described by 0.78 tanks (CSTRs) in series. The fact that the fitted N values are not whole numbers reveals ideality deviations of the spectroscopic cells when modeled as flow reactors. The most effective result is $N = 0.78$ for the Linkam cell reactor (not even one CSTR), which still exhibits deviations between the model and experimental data at high conversions (high spacetimes). Based on the apparent recirculation phenomenon inside the cells, the kinetic data measured in the cell reactors can be described by a model consisting of a PFR with recirculation as follows [53]:

$$X = \frac{1 - e^{-\frac{11.6\frac{W}{F_0}}{R+1}}}{\frac{R}{R+1} - e^{-\frac{11.6\frac{W}{F_0}}{R+1}}} \tag{20}$$

where R is the recirculation ratio. Eq. (20) also satisfactorily describes the kinetic data obtained in the Specac cell reactor (dotted gray curve in Fig. 8d) for $R = 1$, and in the Linkam at low conversions only.

These outcomes are indicative of a non-kinetic controlled regime at low flowrates (and high spacetimes). In this point we need to assign this to (i) bypassing phenomenon, part of the flow that enters the cell moves almost directly to the outlet without contacting the area where the catalyst disc is placed, (ii) dead/stagnant volume zones, part of the fluid is retained in non-active areas and remains in the system for longer than initially expected, reducing the reaction rate; or (iii) mass transfer limitations. We can use the computational fluid dynamics simulations and residence time distribution results to indicate that the mixing is relatively good at high flowrates where it is unlikely that the first two phenomena occur. However, we required a much deeper study of the external and internal mass transfer limitations.

3.3. External mass transfer analysis

The observed effect of lower conversions than expected at high spacetimes ($W/F_0 > 0.2$ g h mol^{-1}) should not be related to a change in the reactor type. As discussed in Figs. 4a-b, there are no significant changes in the mixing behavior of the reactors as the flowrate (F_0) changes. Remember that the weight of the catalyst is kept constant ($W =$ 12 mg) due to a variety of reasons, including having a sufficiently thin disc for the transmission spectroscopic techniques to be used. The lower conversion than expected should be due to an external mass transfer limitation that occurs at very low flowrates. As proved by computational fluid dynamics (Figs. 5 and 6), in these conditions of low flowrates, the linear velocities across the cell reactors are very low, and the convection is minimal.

To determine the existence of a significant resistance for the mass transfer on the boundary layer of the catalyst disc, we estimated the relative decrease on the mole fraction of reactants ($\Delta y/y$) between the bulk area and the catalyst surface at the different spacetimes. These estimations are conducted for the Linkam cell reactor, assuming a behavior of a well-mixed system (CSTR reactor) and the first-order kinetic constant of 11.6 mol g^{-1}h^{-1} previously obtained when the data of the packed-bed reactor were fitted to Eq. (18). Hence, the amount of reactants that is being converted according to the mass-balance, which depends on the inlet (y_{M0}) and outlet (y_M) mole fraction of reactants, has to be equal to the amount of reactants that react, which depends on the mole fraction of reactants on the catalyst disc (y_{Ms}).

$$\dot{n}_M = F_0(y_{M0} - y_M) = F_0 y_{M0} X = kW y_{Ms} \tag{21}$$

$$\Delta y \Big/ y = \frac{(y_M - y_{Ms})}{y_M} \tag{22}$$

The results show (Figure S3) that the external mass transfer resistance can be considered negligible for low spacetimes ($W/F_0 < 0.2$ g h mol^{-1}) when the reactants are introduced in a diluted form ($y_{M0} =$ 0.05), as the relative decrease in the mole fraction of the reactant between the bulk area and the surface is below 5%. Nevertheless, even lower spacetimes are required ($W/F_0 < 0.1$ g h mol^{-1}) when higher concentrations of reactants are used in the inlet ($y_{M0} = 0.16$), as the increase on reaction rate also forces an increase in the transfer rate in order for the latter not to become the limiting one or a phenomenon with a significant contribution. These results explain the lower conversions observed at high spacetimes.

The observable mole concentration mass transfer coefficient (k_c) is estimated using the previous results since the amount of reactant that reacts on the catalyst surface has to be equal to the one that is being transferred from the bulk zone to the catalyst surface. Moreover, the *Sh*, *Re*, and *Bo* dimensionless numbers are estimated starting from the coefficient and assuming that the transfer takes place in laminar regime in a flat plate, although the complex geometry of the Linkam cell and the velocity profiles through the cell that are observed in Fig. 6 suggest being cautious with the numerical values.

$$\dot{n}_M = k_c \frac{P}{RT} A(y_M - y_{Ms}) \tag{23}$$

$$Sh = \frac{k_c L}{D_{i,m}} \tag{24}$$

$$Sh = 0.664 \cdot \mathrm{Re}^{1/2} \cdot Sc^{1/3} \tag{25}$$

$$Bo = \mathrm{Re} \cdot Sc \tag{26}$$

Figure S4 shows the variation of the mass transfer coefficient (k_c) and *Bo* values in regards to the flowrate (F_0). As expected, both parameters increase with increasing flowrates. The values for the Bodenstein dimensionless number, in terms of order of magnitude, suggest that for low flowrates ($F_0 < 0.01$ mol h^{-1}) the flow model that should be considered would be a mixed regime between a pure convection model and the diffusion model, whereas a pure convection model can be assumed for the highest flowrates.

3.4. Internal mass transfer limitations

One of the observations in the experiments in the Linkam cell reactor is the plausible occurrence of internal mass transfer limitations predominantly due to the cell configuration. Note that both sides of the catalyst disc are exposed to the gas flow in the Specac cell reactor. In contrast, only one side of the disc is in direct contact with the gas flow in the Linkam cell reactor, whereas the other side is in contact with the heating element. This configuration for the Linkam cell reactor makes part of the catalyst surface unavailable for direct contact with the gas phase. Therefore, it generates a potential resistance for the diffusion of gas-phase components into the catalyst.

Additionally, the porosity of the pressed disc will be significantly lower than the powder catalytic particles. To prove that, we carried out specific measurements as for example, the N_2 adsorption and desorption capacity of the powder and pressed disc catalysts. Table 1 lists the results for the BET and microporous specific surface areas and volumes for the catalyst in the forms of powder and a pressed disc. The BET surface area and total volume of pores decrease for the catalyst in the form of the pressed disc by 16.5% and 30.2%, respectively. Likewise, the microporous specific surface area and volume decrease by 7.0% and 6.0%,

Table 1
Textural properties of the catalyst in the forms of powder and a pressed disc.

	s_{BET} (m^2 g^{-1})	s_{micro} (m^2 g^{-1})	υ_{total} (m^3 g^{-1})	υ_{micro} (m^3 g^{-1})
Powder	291	130	0.372	$5.63 \cdot 10^{-2}$
Pressed disc	243	121	0.259	$5.29 \cdot 10^{-2}$

respectively, for the catalyst in a pressed disc. This result indicates that the compaction of catalyst powder partially hinders the adsorption of N_2 into the catalyst surface, with more influence on the mesoporous surface. However, the high availability of the microporous surface in the pressed catalyst disc compared to the powder catalyst would not significantly affect the reaction, although reducing the mesoporous surface may affect the diffusion to and from the micropores.

The second set of experiments consisted of an MTH reaction in the Linkam cell reactor using different catalyst weights (W = 12 to 48 mg) and flowrates (F_{M0} = 1.88 to 7.50·10^{-3} to mol h^{-1} or F_0 = 3.75·10^{-2} to 1.50·10^{-1} mol h^{-1}) to obtain the same spacetime (W/F_{M0} = 6.4 g h mol^{-1} or W/F_0 = 0.32 g h mol^{-1}). This experiment would lead to similar results if no internal mass transfer limitations existed. Fig. 9 presents the kinetic results in terms of the time-on-stream evolution of the conversion (Fig. 9a) and the yield of LOs against conversion in Fig. 9b. The different results for both experiments indicate the existence of internal mass transfer limitations in the catalyst disc. The conversion levels are lower for the experiment using a thicker catalyst disc (48 mg) than for the standard experiment with a thinner catalyst disc (12 mg), regardless of the same theoretical spacetime (0.32 g h mol^{-1}). Compared with an experiment using a methanol flowrate of 7.5·10^{-3} mol h^{-1} and a thinner catalyst disc (12 mg) with a lower spacetime (W/F_0 = 0.08 g h mol^{-1}), the conversion levels are lower but closer to the experiment with the thicker catalyst disc.

To further support the existence of internal mass transfer limitations, the thicker spent catalyst disc was studied by analyzing the transversal disc section (as indicated in Fig. 10) with elemental mapping of carbon using SEM-EDS. The SEM-EDS images for the elemental analysis of carbon reveal the presence of carbonaceous species on the disc surface (Figs. 10a-b), whereas little to no presence of carbonaceous species exists across the transversal disc section (Fig. 10c). The semi-quantitative analysis of carbon using EDS provides a profile of carbonaceous species

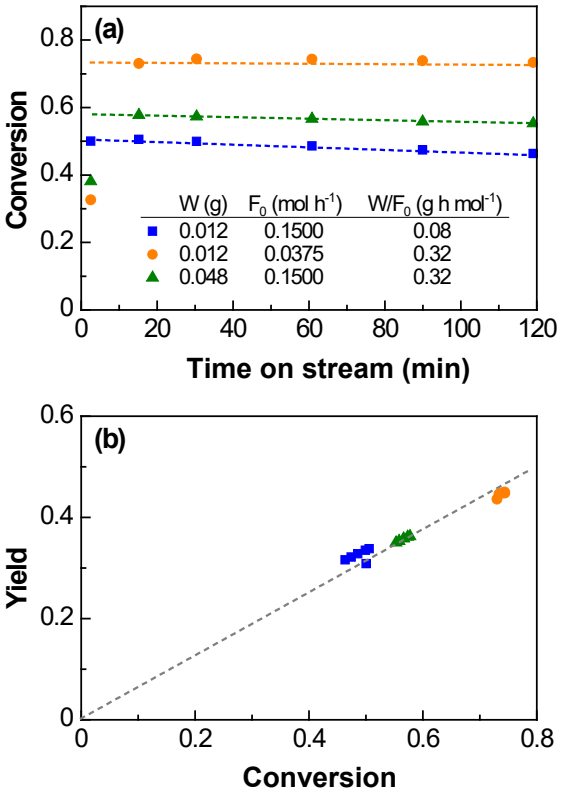

Fig. 9. Kinetic performance for experiments with different catalyst disc weights for the methanol-to-hydrocarbon reaction in the Linkam cell reactor: (a) time-on-stream evolution of the conversion and (b) light olefin yield.

across the transversal disc section, confirming the abundance of these species on the disc surface. In contrast, the species are negligible inside the disc. These observations verify that the reactants or products could not reach the inner catalyst particles in the disc; therefore, carbonaceous compounds could not be formed. This problem can be partially solved using thin pressed catalyst samples (W = 12 mg), as used for most experiments presented in this work.

To establish a limiting mass of the catalyst disc that should be used in this reaction system without significant internal mass transfer limitations, we estimated the effective porosity in the catalyst disc and calculated the effectiveness using the Thiele module that would match the conversions obtained when the 12 and 48 mg discs were used at the same theoretical spacetime (0.32 g h mol^{-1}). The calculation procedure is explained in the Supplementary Information, from which an effective porosity of 0.114 was estimated, which gives way to effectiveness values of 0.979 and 0.760 for the 12 and 48 mg discs, respectively. The results suggest that the 12 mg disc used in the experiments of this study is adequate to prevent significant internal mass transfer limitations (for this catalyst disc surface and these intrinsic kinetics), whereas the 48 mg catalyst is not, as it is observed in Fig. 9. A limiting value of 19 mg of catalyst disc is suggested to prevent internal mass transfer resistances that would represent > 5% of the total resistance (Figure S5).

3.5. Deactivation performance

The experiments in the spectroscopic cells and packed-bed reactor were carried out for a determined time to assess the conversion evolution with the time on stream (Fig. 11). The experiments at y_{M0} = 0.85 in the packed-bed reactor (Fig. 11a) and at y_{M0} = 0.16 in the Specac (Fig. 11b) and Linkam cell reactors (Fig. 11c) reveal that the conversion decays over the time on stream, indicating partial catalyst deactivation. In contrast, this decay is not observed (or is negligible) at y_{M0} = 0.05 in the Linkam cell reactor (Fig. 11d). Generally, the conversion decay is more pronounced at low spacetimes, which is logical because of a higher concentration of reactant/products for the same catalyst amount at a given time on stream.

The catalyst deactivation in a packed-bed reactor for the MTH reaction mainly occurs by coke formed from the reactants (oxygenates) and products (hydrocarbons) [14,27]. Therefore, a model depending on the concentration of both reactants (oxygenates, $y_M = y_{M0}(1 - X)$) and products (hydrocarbons, $y_H = y_{M0}X$) is appropriate to describe these deactivation profiles (conversion against time on stream):

$$-\frac{dX}{dt} = k_d {y_{M0}}^2 (1 - X)X \tag{27}$$

Solving with the limits ($t = 0, X = X_0$) and ($t = t_{end}, X = X_{end}$), where X_0 is the conversion in steady-state conditions determined from the autocatalytic kinetic model (Fig. 8b), we obtain the following:

$$X = \frac{X_0 e^{-k_d {y_{M0}}^2 t}}{1 + X_0 (e^{-k_d {y_{M0}}^2 t} - 1)} \tag{28}$$

As expected, this model satisfactorily describes the deactivation behavior observed in the packed-bed reactor, providing a k_d value of 7.2·10^{-3} min^{-1}. However, this model does not satisfactorily describe the deactivation profiles observed in the spectroscopic cells. To quantify the deactivation in each spectroscopic cell, we propose a simple deactivation model based on the concentration of reactants (oxygenates, $y_M = y_{M0}(1 - X)$):

$$-\frac{dX}{dt} = k_d y_{M0} (1 - X) \tag{29}$$

where k_d is the deactivation coefficient. Eq. (29) is solved for the limits ($t = 0, X = X_0$) and ($t = t_{end}, X = X_{end}$), where X_0 is the conversion at steady-state conditions determined from the model of N tanks in series (Fig. 8d), resulting in:

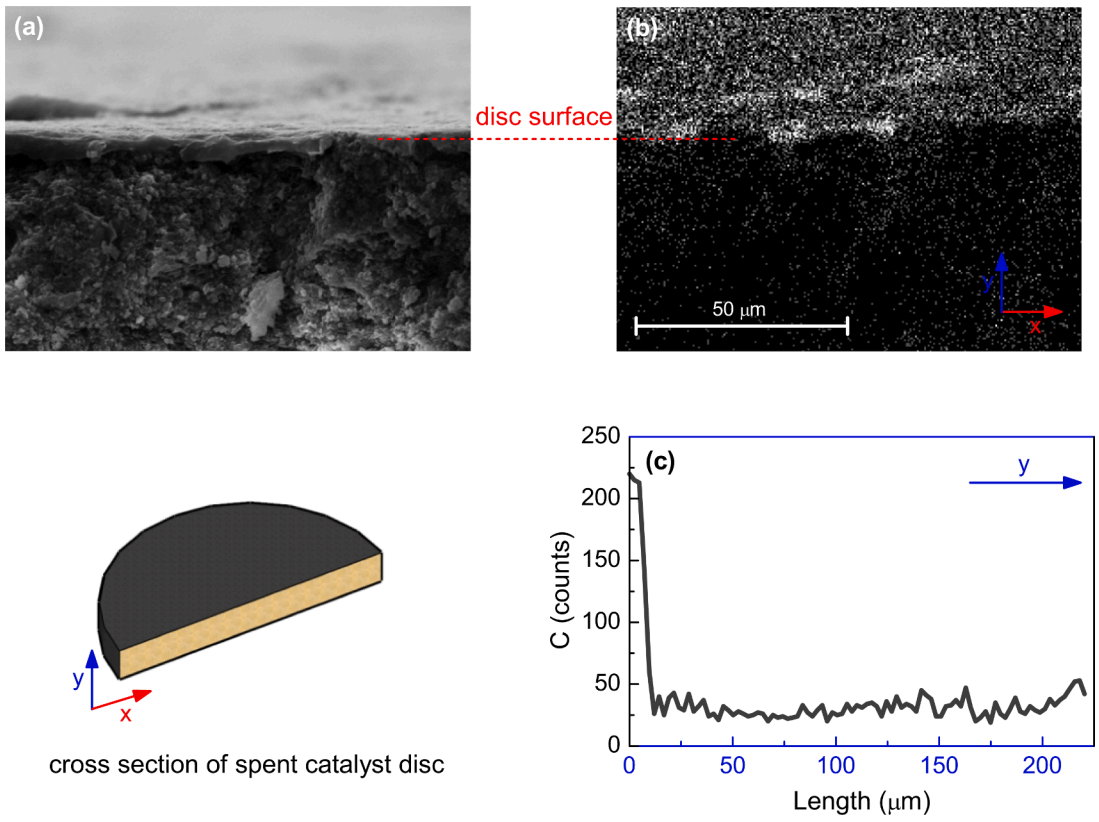

Fig. 10. Scanning electron microscopy (SEM) energy-dispersive x-ray spectroscopy (EDS) analysis of a spent catalyst disc used in the methanol-to-hydrocarbon reaction in the Linkam cell reactor: (a) SEM image, (b) C map from the EDS analysis, (c) C counts across the catalyst disc section.

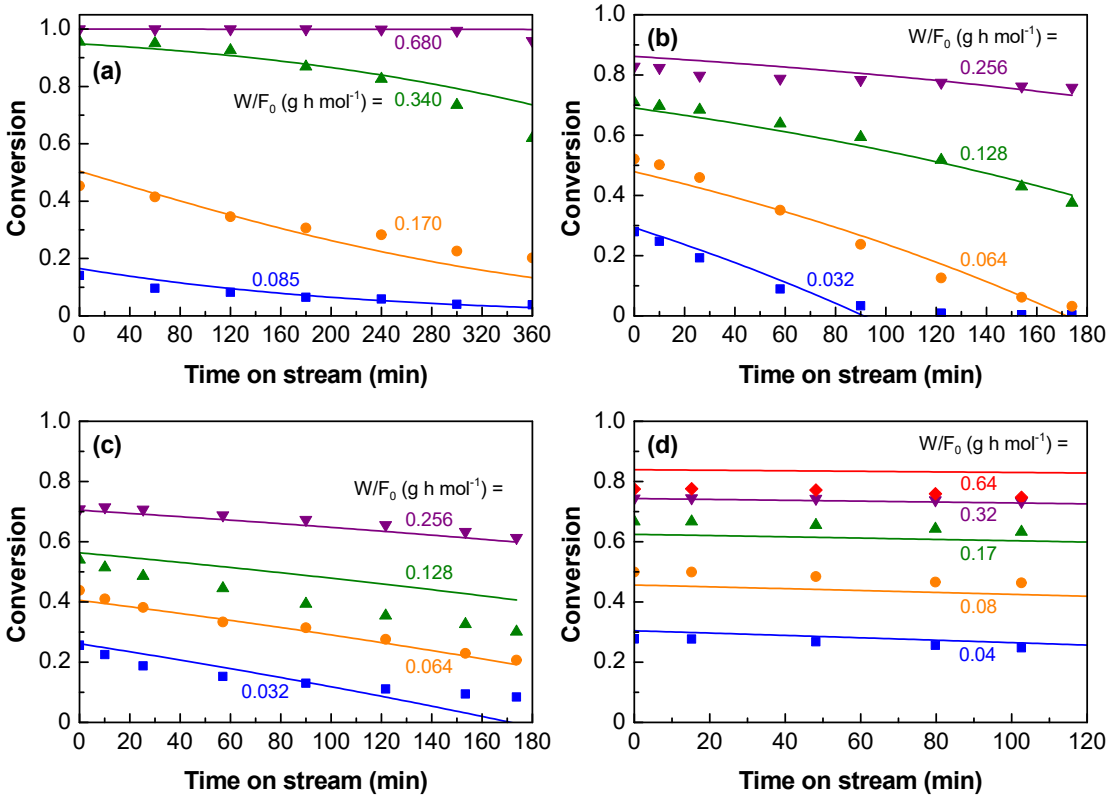

Fig. 11. Deactivation profiles for the methanol-to-hydrocarbon reaction at 400 °C in the three reaction systems: (a) packed-bed reactor at $y_{M0} = 0.85$, (b) Specac cell reactor at $y_{M0} = 0.16$, (c) Linkam cell reactor at $y_{M0} = 0.16$, and (d) the same at $y_{M0} = 0.05$.

$$X = 1 - (1 - X_0)e^{k_d y_{M0} t} \quad (30)$$

Figs. 11b-c (solid lines) illustrate that this model satisfactorily describes the deactivation behavior observed in spectroscopic cells, resulting in k_d values of $2.37{\cdot}10^{-2}$ min^{-1} for the Specac cell reactor and $1.10{\cdot}10^{-2}$ min^{-1} for the Linkam cell reactor. The use of different models to describe the deactivation behavior of the packed-bed reactor and spectroscopic cells implies other deactivation mechanisms. In the packed-bed system, the catalyst undergoes deactivation due to coke formation from oxygenates and hydrocarbons. This outcome is consistent with the progressive deactivation of the catalytic bed by forming primary coke from methanol and secondary coke from olefins (series–parallel deactivation mechanism) [27]. Instead, the catalyst deactivation in spectroscopic cells primarily depends on the concentration of oxygenates, implying the deactivating species are primarily formed from oxygenates suggesting a parallel deactivation mechanism.

Since the data are represented using different models, comparing the k_d values for the packed-bed reactor and spectroscopic cells is not straightforward. The deactivation model for the packed-bed reactor is a second-order model; therefore, the k_d value would implicitly have squared units. Thus, taking the square root of the k_d value for the packed-bed reactor results in $8.48{\cdot}10^{-2}$, suggesting that the deactivation would be faster in the packed-bed reactor than in the spectroscopic cells (with k_d values of $1.10{\cdot}10^{-2}$ to $2.37{\cdot}10^{-2}$). Müller at al. [59] reported a similar observation when comparing the catalyst deactivation in a PFR and CSTR for the MTH reaction, finding that it is faster in the PFR, which is attributable to a change in the deactivation mechanism in both systems.

4. Discussions

The results presented so far can be summarized in Fig. 12 showing the overall framework to assess the kinetic information obtained in spectroscopic cell reactors. The main goal is measuring intrinsic kinetics in these reactors, in the absence of fluid dynamic abnormalities and mass transfer limitations. In the commercial cells used in this work, the temperature is well controlled across the disc but not all the instruments perform in the same way [32,62,63]. The basic rule to approach the intrinsic kinetic regime is working in differential reaction conditions: low catalyst loading (thin catalyst discs), high flowrates, low fraction of reactants ($y_{reactants}$), high fraction of inerts (y_{inerts}), and mild conditions of temperature and pressure to drop the overall kinetic rate and make it more significant as compared to other phenomena. Accordingly, the main findings of this work can be summarized as follows:

- Low catalyst loadings are needed to obtain thin discs (considering the catalyst disc area is constant), which has positive outcomes by lowering the internal mass transfer resistances and improving the transmittance when required by the spectroscopic technique. In our case, we found that working with 12 mg of catalyst in 1.3 cm diameter discs is a satisfactory strategy to meet these outcomes.
- High flowrates are needed to lower the contact time and the conversion and to improve mixing and convection. This suppresses the fluid dynamic abnomalies such as bypass and dead/stagnant volume zones while lowering the external mass transfer resistances. With these effects combined, the reactors approach the intrinsic kinetic regime. In our case, we achieved a perfect mixing behavior (or combinations of a few CSTRs in series) working at $F_0 > 0.06$ mol h^{-1}.

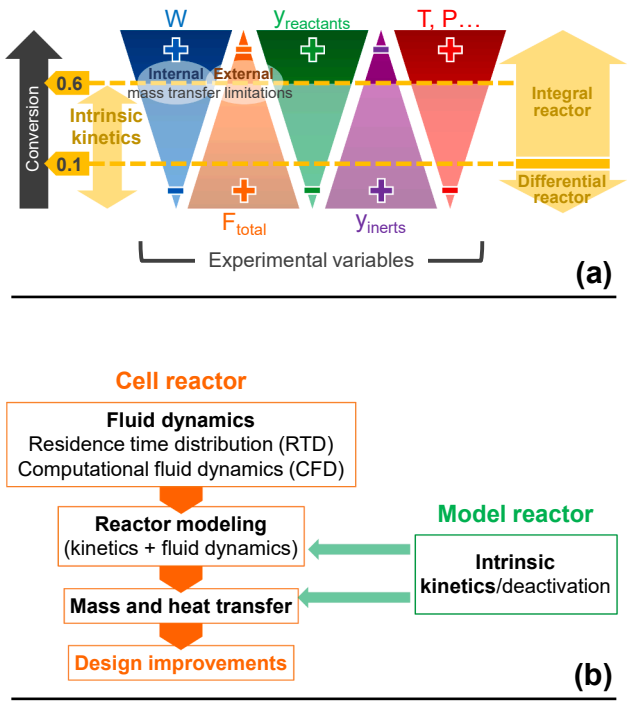

Fig. 12. Study of cell reactors: (a) effect of experimental variables on the cell reactor performance; (b) framework for the analysis of cell reactors.

As demonstrated, the spectroscopic cell reactors approach to a perfect mixing behavior instead of plug flow, which could be of interest for research purposes. As long as the reactor behavior is within some limits that approach an ideal behavior, we can estimate the observed kinetics using the intrinsic kinetic data obtained in a reference reactor (in our case, a packed-bed reactor). This approach is very much needed in order to understand how far the conditions used are from this regime.

Based on the experimental design and findings of this work, Fig. 12b shows the overall framework to assess the adequacy of spectroscopic cells operating as gas–solid reactors. Accordingly, three basic analysis steps must be considered: fluid dynamics, reactor modeling (kinetics viewpoint), and mass and heat transfer limitations.

The fluid dynamic analysis must be focused on determining the flow regimes by running residence time distribution experiments and computational fluid dynamics simulations. With the residence time distribution experiments, the characterization of the reactor with relatively simple expressions is possible. However, these are not useful to scale up or to propose design (or condition) improvements because they are specific features of the reactor. Complementarily, computational fluid dynamics simulations enhance the understanding of the fluid distribution in the reactor or the fluid dynamic abnormalities (e.g., bypass or dead/stagnant volume zones) and they are a powerful tool to propose these design improvements [64]. Our results show that computational fluid dynamics simulations are not able to fully capture the fluid pattern inside the cell reactors given the discrepancy with the residence time distribution experimental results and the intricate internals of the cells that seem to cause fluid dynamic abnormalities. In this work, we have not proposed such modifications as we aimed the experimental conditions to reach the intrinsic kinetic conditions.

The analysis step of reactor modeling comprises carrying out kinetic tests in the cell reactors, for which is necessary to know the intrinsic kinetics obtained in a model reactor as previously mentioned. Knowing both, the kinetic and fluid dynamic performances, a simple, reliable, representative and extrapolative reactor model can be approached.

Finally, the last analysis step requires a good assessment of the internal and external mass transfer limitations with the proper dimensionless numbers. The results of this work show that both fluid dynamic abnormalities and mass transfer limitations may occur simultaneously at high catalyst loadings (thick catalyst disc) and low flowrates. The internal mass transfer limitations occur at high catalyst loadings since the disc area must be constant to fit in the cell making the thickness increase and causing diffusion limitations due to the compaction of the catalyst particles. Going to the first point, having an intrinsic kinetic model

obtained in a reference reactor is instrumental to assess the effect of all these limitations. From the side of the deactivation, these reactors seem good candidates for such studies.

5. Conclusions

To assess the performance of the commercial Specac and Linkam gas–solid cell reactors as reactors, we have developed a complete spectro-kinetic-fluid dynamic framework. Here we performed experiments to investigate the residence time distribution, kinetics, deactivation, and mass transfer behaviors. Fluid dynamic simulations validated by comparison with these experiments predicted flow patterns and velocity distributions inside the cells.

The residence time distribution curves suggest that the flow performance in the cells is closer to a few ideal CSTRs in series. The simulated flow patterns and velocity distributions under the reaction conditions indicate a back-mixing phenomenon, confirming the close resemblance of the cells to continuously stirred tanks.

We demonstrated that these commercial spectroscopic cells are suitable as reactors for the MTH reaction to monitor the in situ formation and degradation as well as to obtain kinetic information for the species. The results were compared with those obtained in a packed-bed reactor to verify the consistency of the kinetic observations. The kinetic data from the spectroscopic cells for the MTH reaction were described using a first-order kinetic model for a determined number of tanks in series, in sharp contrast with the autocatalytic model for the kinetic data obtained in the packed-bed reactor. However, these behaviors can only be attained in certain operational regions: low catalyst loadings (thin catalyst discs), high flowrates, low partial pressure of reactants, and mild conditions of temperature and pressure. With that, we approach to a differential reactor and the intrinsic kinetic regimes, and we can neglect fluid dynamic misdistributions (such as bypasses or dead volume zones) or mass transfer limitations.

According to the high back-mixing in the cell reactors used, the induction step of the reaction was suppressed, accelerating the apparent reaction rate obtained in the packed-bed reactor. In addition to the experiments, we provide a complete framework to prevent any misleading regime and operate these systems at the best conditions.

Declaration of Competing Interest

The authors declare that they have no known competing financial interests or personal relationships that could have appeared to influence the work reported in this paper.

Data availability

Data will be made available on request.

Acknowledgments

This work was possible due to the financial support of the Ministry of Economy, Industry, and Competitiveness of the Spanish Government (project CTQ2016-79646-P, cofounded with ERDF funds), the Basque Government (projects IT1218-19 and IT1645-22), and the King Abdullah University of Science and Technology (KAUST, project BAS/1/1403). J.V. is grateful for the fellowship granted by the Ministry of Economy, Industry, and Competitiveness of the Spanish Government (BES-2014-069980). The authors are grateful for the technical and human support provided by IZO-SGI SGIker of the University of the Basque Country (UPV/EHU) and European funding (ERDF and ESF).

Appendix A. Supplementary data

Supplementary data to this article can be found online at https://doi.org/10.1016/j.cej.2022.137865.

References

[1] E. Borodina, F. Meirer, I. Lezcano-González, M. Mokhtar, A.M. Asiri, S.A. Al-Thabaiti, S.N. Basahel, J. Ruiz-Martinez, B.M. Weckhuysen, Influence of the reaction temperature on the nature of the active and deactivating species during methanol to olefins conversion over H-SSZ-13, ACS Catal. 5 (2015) 992–1003, https://doi.org/10.1021/cs501345g.

[2] K. De Wispelaere, C.S. Wondergem, B. Ensing, K. Hemelsoet, E.J. Meijer, B. M. Weckhuysen, V. Van Speybroeck, J. Ruiz-Martínez, Insight into the Effect of Water on the Methanol-to-Olefins Conversion in H-SAPO-34 from Molecular Simulations and in Situ Microspectroscopy, ACS Catal. 6 (2016) 1991–2002, https://doi.org/10.1021/acscatal.5b02139.

[3] X. Peng, D. Kulkarni, Y. Huang, T.J. Omasta, B. Ng, Y. Zheng, L. Wang, J. M. LaManna, D.S. Hussey, J.R. Varcoe, I.V. Zenyuk, W.E. Mustain, Using operando techniques to understand and design high performance and stable alkaline membrane fuel cells, Nat. Commun. 111 (11) (2020) 1–10, https://doi.org/10.1038/s41467-020-17370-7.

[4] H. Wang, D.J. Kline, M.R. Zachariah, In-operando high-speed microscopy and thermometry of reaction propagation and sintering in a nanocomposite, Nat. Commun. 101 (10) (2019) 1–8, https://doi.org/10.1038/s41467-019-10843-4.

[5] G. Abdulkareem-Alsultan, N. Asikin-Mijan, L.K. Obeas, R. Yunus, S.Z. Razali, A. Islam, Y., Hin Taufiq-Yap, In-situ operando and ex-situ study on light hydrocarbon-like-diesel and catalyst deactivation kinetic and mechanism study during deoxygenation of sludge oil, Chem. Eng. J. 429 (2022), 132206, https://doi.org/10.1016/J.CEJ.2021.132206.

[6] J. Ding, H. Zheng, H. Gao, S. Wang, S. Wu, S. Fang, F. Cheng, Operando non-topological conversion constructing the high-performance nickel-zinc battery anode, Chem. Eng. J. 414 (2021), 128716, https://doi.org/10.1016/J.CEJ.2021.128716.

[7] Y. Wu, Y. Li, M. Yuan, H. Hao, X. San, Z. Lv, L. Xu, B. Wei, Operando capturing of surface self-reconstruction of Ni3S2/FeNi2S4 hybrid nanosheet array for overall water splitting, Chem. Eng. J. 427 (2022), 131944, https://doi.org/10.1016/J.CEJ.2021.131944.

[8] M.A. Ali, S. Ahmed, N. Al-Baghli, Z. Malaibari, A. Abutaleb, A. Yousef, A Comprehensive review covering conventional and structured catalysis for methanol to propylene conversion, Catal. Letters. 149 (2019) 3395–3424, https://doi.org/10.1007/s10562-019-02914-4.

[9] E. Ebadzadeh, M.H. Khademi, M. Beheshti, A kinetic model for methanol-to-propylene process in the presence of co-feeding of C4–C5 olefin mixture over H-ZSM-5 catalyst, Chem. Eng. J. 405 (2021), 126605, https://doi.org/10.1016/J.CEJ.2020.126605.

[10] S. Standl, F.M. Kirchberger, T. Kühlewind, M. Tonigold, M. Sanchez-Sanchez, J. A. Lercher, O. Hinrichsen, Single-event kinetic model for methanol-to-olefins (MTO) over ZSM-5: Fundamental kinetics for the olefin co-feed reactivity, Chem. Eng. J. 402 (2020), 126023, https://doi.org/10.1016/J.CEJ.2020.126023.

[11] X. Fan, Y. Jiao, Porous Materials for Catalysis: Toward Sustainable Synthesis and Applications of Zeolites, Sustain. Nanoscale Eng. From Mater. Des. to, Chem. Process. (2020) 115–137, https://doi.org/10.1016/B978-0-12-814681-1.00005-9.

[12] I. Yarulina, A.D. Chowdhury, F. Meirer, B.M. Weckhuysen, J. Gascon, Recent trends and fundamental insights in the methanol-to-hydrocarbons process, Nat. Catal. 1 (2018) 398–411, https://doi.org/10.1038/s41929-018-0078-5.

[13] J.L. White, Methanol-to-hydrocarbon chemistry: The carbon pool (r)evolution, Catal, Sci. Technol. 1 (2011) 1630–1635, https://doi.org/10.1039/c1cy00197c.

[14] U. Olsbye, S. Svelle, K.P. Lillerud, Z.H. Wei, Y.Y. Chen, J.F. Li, J.G. Wang, W.B. Fan, The formation and degradation of active species during methanol conversion over protonated zeotype catalysts, Chem. Soc. Rev. 44 (2015) 7155–7176, https://doi.org/10.1039/c5cs00304k.

[15] P. Tian, Y. Wei, M. Ye, Z. Liu, Methanol to olefins (MTO): From fundamentals to commercialization, ACS Catal. 5 (2015) 1922–1938, https://doi.org/10.1021/acscatal.5b00007.

[16] S. Ilias, A. Bhan, Mechanism of the catalytic conversion of methanol to hydrocarbons, ACS Catal. 3 (2013) 18–31, https://doi.org/10.1021/cs3006583.

[17] J. Zhu, Y. Li, U. Muhammad, D. Wang, Y. Wang, Effect of alkene co-feed on the MTO reactions over SAPO-34, Chem. Eng. J. 316 (2017) 187–195, https://doi.org/10.1016/J.CEJ.2017.01.090.

[18] D. Mier, A.T. Aguayo, A.G. Gayubo, M. Olazar, J. Bilbao, Synergies in the production of olefins by combined cracking of n-butane and methanol on a HZSM-5 zeolite catalyst, Chem. Eng. J. 160 (2010) 760–769.

[19] Z. Shi, S.S. Arora, D.W. Trahan, D. Hickman, A. Bhan, Methanol to hydrocarbons conversion: Why dienes and monoenes contribute differently to catalyst deactivation? Chem. Eng. J. (2021), 134229 https://doi.org/10.1016/J.CEJ.2021.134229.

[20] D. Mores, J. Kornatowski, U. Olsbye, B.M. Weckhuysen, Coke formation during the methanol-to-olefin conversion: In situ microspectroscopy on individual H-ZSM-5 crystals with different brønsted acidity, Chem. - A Eur. J. 17 (2011) 2874–2884, https://doi.org/10.1002/chem.201002624.

[21] D. Mores, E. Stavitski, M.H.F. Kox, J. Kornatowski, U. Olsbye, B.M. Weckhuysen, Space- And time-resolved in-situ spectroscopy on the coke formation in molecular sieves: Methanol-to-olefin conversion over H-ZSM-5 and H-SAPO-34, Chem. - A Eur. J. 14 (2008) 11320–11327, https://doi.org/10.1002/chem.200801293.

[22] J. Valecillos, E. Epelde, J. Albo, A.T. Aguayo, J. Bilbao, P. Castaño, Slowing down the deactivation of H-ZSM-5 zeolite catalyst in the methanol-to-olefin (MTO) reaction by P or Zn modifications, Catal. Today. (2019), https://doi.org/10.1016/j.cattod.2019.07.059.

[23] J. Valecillos, G. Elordi, A.T. Aguayo, P. Castaño, The intrinsic effect of co-feeding water on the formation of active/deactivating species in the methanol-to-

hydrocarbons reaction on ZSM-5 zeolite, Catal, Sci. Technol. 11 (2021) 1269–1281, https://doi.org/10.1039/D0CY02497J.
[24] J. Valecillos, J. Ruiz-Martinez, A.T. Aguayo, P. Castaño, Combined Ex and In Situ Measurements Elucidate the Dynamics of Retained Species in ZSM-5 and SAPO-18 Catalysts Used in the Methanol-to-Olefins Reaction, Chem. – A Eur. J. 27 (2021) 6719–6731, https://doi.org/10.1002/chem.202004865.
[25] F. Huang, J. Cao, L. Wang, X. Wang, F. Liu, Enhanced catalytic behavior for methanol to lower olefins over SAPO-34 composited with ZrO2, Chem. Eng. J. 380 (2020), 122626, https://doi.org/10.1016/J.CEJ.2019.122626.
[26] Q. Qian, J. Ruiz-Martínez, M. Mokhtar, A.M. Asiri, S.A. Al-Thabaiti, S.N. Basahel, H.E. Van Der Bij, J. Kornatowski, B.M. Weckhuysen, Single-particle spectroscopy on large SAPO-34 crystals at work: Methanol-to-olefin versus ethanol-to-olefin processes, Chem. - A Eur. J. 19 (2013) 11204–11215, https://doi.org/10.1002/chem.201300540.
[27] J. Goetze, B.M. Weckhuysen, Spatiotemporal coke formation over zeolite ZSM-5 during the methanol-to-olefins process as studied with: Operando UV-vis spectroscopy: A comparison between H-ZSM-5 and Mg-ZSM-5, Catal, Sci. Technol. 8 (2018) 1632–1644, https://doi.org/10.1039/c7cy02459b.
[28] Q. Qian, J. Ruiz-Martínez, M. Mokhtar, A.M. Asiri, S.A. Al-Thabaiti, S.N. Basahel, B.M. Weckhuysen, Single-catalyst particle spectroscopy of alcohol-to-olefins conversions: Comparison between SAPO-34 and SSZ-13, Catal. Today. 226 (2014) 14–24, https://doi.org/10.1016/j.cattod.2013.09.056.
[29] K. Hemelsoet, Q. Qian, T. De Meyer, K. De Wispelaere, B. De Sterck, B. M. Weckhuysen, M. Waroquier, V. Van Speybroeck, Identification of intermediates in zeolite-catalyzed reactions by in situ UV/Vis microspectroscopy and a complementary set of molecular simulations, Chem. - A Eur. J. 19 (2013) 16595–16606, https://doi.org/10.1002/chem.201301965.
[30] M.A. Bañares, Operando methodology: combination of in situ spectroscopy and simultaneous activity measurements under catalytic reaction conditions, Catal. Today. 100 (2005) 71–77. https://doi.org/10.1016/j.cattod.2004.12.017.
[31] M.A. Bañares, Operando spectroscopy: The knowledge bridge to assessing structure-performance relationships in catalyst nanoparticles, Adv. Mater. 23 (2011) 5293–5301, https://doi.org/10.1002/adma.201101803.
[32] F.C. Meunier, The design and testing of kinetically-appropriate operando spectroscopic cells for investigating heterogeneous catalytic reactions, Chem. Soc. Rev. 39 (2010) 4602–4614, https://doi.org/10.1039/b919705m.
[33] C.O. Arean, B.M. Weckhuysen, A. Zecchina, Operando surface spectroscopy—placing catalytic solids at work under the spotlight, Phys. Chem. Chem. Phys. 14 (2012) 2125, https://doi.org/10.1039/c2cp90005j.
[34] B.M. Weckhuysen, In situ Spectroscopy of Catalysts, ChemInform. 36 (2005), https://doi.org/10.1002/chin.200523297.
[35] M. Hunger, Applications of in situ spectroscopy in zeolite catalysis, Microporous Mesoporous Mater. 82 (2005) 241–255, https://doi.org/10.1016/j.micromeso.2005.01.037.
[36] M. Hunger, M. Seiler, A. Buchholz, In situ MAS NMR spectroscopic investigation of the conversion of methanol to olefins on silicoaluminophosphates SAPO-34 and SAPO-18 under continuous flow conditions, Catal. Letters. 74 (2001) 61–68, https://doi.org/10.1023/A:1016687014695.
[37] A.T. Aguayo, A.G. Gayubo, R. Vivanco, A. Alonso, J. Bilbao, Initiation step and reactive intermediates in the transformation of methanol into olefins over SAPO-18 catalyst, Ind. Eng. Chem. Res. 44 (2005) 7279–7286, https://doi.org/10.1021/ie040291a.
[38] W. Dai, X. Wang, G. Wu, L. Li, N. Guan, M. Hunger, Methanol-to-Olefin Conversion Catalyzed by Low-Silica AlPO-34 with Traces of Brønsted Acid Sites: Combined Catalytic and Spectroscopic Investigations, ChemCatChem 4 (2012) 1428–1435, https://doi.org/10.1002/cctc.201100503.
[39] W. Dai, G. Wu, L. Li, N. Guan, M. Hunger, Mechanisms of the deactivation of SAPO-34 materials with different crystal sizes applied as MTO catalysts, ACS Catal. 3 (2013) 588–596, https://doi.org/10.1021/cs400007v.
[40] R. Portela, S. Perez-Ferreras, A. Serrano-Lotina, M.A. Bañares, Engineering operando methodology: Understanding catalysis in time and space, Front. Chem. Sci. Eng. 12 (2018) 509–536, https://doi.org/10.1007/s11705-018-1740-9.
[41] Q. Xiong, Y. Yang, F. Xu, Y. Pan, J. Zhang, K. Hong, G. Lorenzini, S. Wang, Overview of Computational Fluid Dynamics Simulation of Reactor-Scale Biomass Pyrolysis, ACS Sustain. Chem. Eng. 5 (2017) 2783–2798, https://doi.org/10.1021/acssuschemeng.6b02634.
[42] S. Thomas, O. Marie, P. Bazin, L. Lietti, C.G. Visconti, M. Corbetta, F. Manenti, M. Daturi, Modelling a reactor cell for operando IR studies: From qualitative to fully quantitative kinetic investigations, Catal. Today. 283 (2017) 176–184, https://doi.org/10.1016/j.cattod.2016.07.008.
[43] M. De Sousa Duarte, M. Rolland, C. Sagnard, D. Suire, F. Flacher, O. Delpoux, C. P. Lienemann, High-Pressure High-Temperature Transparent Fixed-Bed Reactor for Operando Gas-Liquid Reaction Follow-up, Chem. Eng. Technol. 42 (2019) 655–660, https://doi.org/10.1002/ceat.201800090.
[44] X. Gao, T. Li, W.A. Rogers, K. Smith, K. Gaston, G. Wiggins, J.E. Parks, Validation and application of a multiphase CFD model for hydrodynamics, temperature field and RTD simulation in a pilot-scale biomass pyrolysis vapor phase upgrading reactor, Chem. Eng. J. 388 (2020), 124279, https://doi.org/10.1016/J.CEJ.2020.124279.
[45] J. Sen Li, L.T. Zhu, Z.H. Luo, Effect of geometric configuration on hydrodynamics, heat transfer and RTD in a pilot-scale biomass pyrolysis vapor-phase upgrading reactor, Chem. Eng. J. 428 (2022), 131048, https://doi.org/10.1016/J.CEJ.2021.131048.
[46] W. Li, M. Li, Z. Qiang, Improvement of UV disinfection reactor performance by ring baffles: The matching between the hydrodynamics and UV radiation, Chem. Eng. J. 379 (2020), 122381, https://doi.org/10.1016/J.CEJ.2019.122381.
[47] B. Van Tran, S. Ich Ngo, Y. Il Lim, H. Hung Pham, S.H. Lim, K.S. Go, N.S. Nho, Estimation of physical properties and hydrodynamics of slurry bubble column reactor for catalytic hydrocracking of vacuum residue, Chem. Eng. J. 418 (2021), 129378, https://doi.org/10.1016/J.CEJ.2021.129378.
[48] B.S. Patil, P.D. Srinivasan, E. Atchison, H. Zhu, J.J. Bravo-Suárez, Design, modelling, and application of a low void-volume in situ diffuse reflectance spectroscopic reaction cell for transient catalytic studies, React, Chem. Eng. 4 (2019) 667–678, https://doi.org/10.1039/C8RE00302E.
[49] E. Borodina, H. Sharbini Harun Kamaluddin, F. Meirer, M. Mokhtar, A.M. Asiri, S. A. Al-Thabaiti, S.N. Basahel, J. Ruiz-Martinez, B.M. Weckhuysen, Influence of the Reaction Temperature on the Nature of the Active and Deactivating Species during Methanol-to-Olefins Conversion over H-SAPO-34, ACS Catal. 7 (2017) 5268–5281, https://doi.org/10.1021/acscatal.7b01497.
[50] J. Valecillos, Z. Tabernilla, E. Epelde, E. Sastre, A.T. Aguayo, P. Castaño, Quenching the Deactivation in the Methanol-to-Olefin Reaction by Using Tandem Fixed-Beds of ZSM-5 and SAPO-18 Catalysts, Ind. Eng. Chem. Res. 59 (2020) 13892–13905, https://doi.org/10.1021/acs.iecr.0c01616.
[51] J. Valecillos, I. Hita, E. Sastre, A.T. Aguayo, P. Castaño, Implications of Co-Feeding Water on the Growth Mechanisms of Retained Species on a SAPO-18 Catalyst during the Methanol-to-Olefins Reaction, ChemCatChem 13 (2021) 3140–3154. https://doi.org/10.1002/cctc.202100124.
[52] J. Valecillos, H. Vicente, A.G. Gayubo, A.T. Aguayo, P. Castaño, Spectro-kinetics of the methanol to hydrocarbons reaction combining online product analysis with UV–vis and FTIR spectroscopies throughout the space time evolution, J. Catal. 408 (2022) 115–127, https://doi.org/10.1016/J.JCAT.2022.02.021.
[53] O. Levenspiel, Chemical reaction engineering, John Wiley & Sons Ltd, New York, 2004.
[54] H.S. Fogler, Elements of chemical reaction engineering, Fifth edit, Prentice Hall, Philadelphia, PA, PA, 2016.
[55] ANSYS Inc, ANSYS Fluent Theory Guide, Canonsburg, PA, 2020.
[56] ANSYS Inc, Workbench User's Guide, Canonsburg, PA, 2020.
[57] A.G. Gayubo, A.T. Aguayo, A. Alonso, A. Atutxa, J. Bilbao, Reaction scheme and kinetic modelling for the MTO process over a SAPO-18 catalyst, Catal. Today. 106 (2005) 112–117, https://doi.org/10.1016/j.cattod.2005.07.133.
[58] X. Sun, S. Mueller, Y. Liu, H. Shi, G.L. Haller, M. Sanchez-Sanchez, A.C. Van Veen, J.A. Lercher, On reaction pathways in the conversion of methanol to hydrocarbons on HZSM-5, J. Catal. 317 (2014) 185–197, https://doi.org/10.1016/j.jcat.2014.06.017.
[59] S. Müller, Y. Liu, M. Vishnuvarthan, X. Sun, A.C. Van Veen, G.L. Haller, M. Sanchez-Sanchez, J.A. Lercher, Coke formation and deactivation pathways on H-ZSM-5 in the conversion of methanol to olefins, J. Catal. 325 (2015) 48–59, https://doi.org/10.1016/j.jcat.2015.02.013.
[60] T.V.W. Janssens, S. Svelle, U. Olsbye, Kinetic modeling of deactivation profiles in the methanol-to-hydrocarbons (MTH) reaction: A combined autocatalytic-hydrocarbon pool approach, J. Catal. 308 (2013) 122–130, https://doi.org/10.1016/j.jcat.2013.05.035.
[61] T.V.W. Janssens, A new approach to the modeling of deactivation in the conversion of methanol on zeolite catalysts, J. Catal. 264 (2009) 130–137, https://doi.org/10.1016/j.jcat.2009.03.004.
[62] D. Tibiletti, A. Goguet, D. Reid, F.C. Meunier, R. Burch, On the need to use steady-state or operando techniques to investigate reaction mechanisms: An in situ DRIFTS and SSITKA-based study example, Catal. Today. 113 (2006) 94–101, https://doi.org/10.1016/J.CATTOD.2005.11.013.
[63] H. Li, M. Rivallan, F. Thibault-Starzyk, A. Travert, F.C. Meunier, Effective bulk and surface temperatures of the catalyst bed of FT-IR cells used for in situ and operando studies, Phys. Chem. Chem. Phys. 15 (2013) 7321–7327, https://doi.org/10.1039/c3cp50442e.
[64] A. Carías-Henriquez, S. Pietrzyk, C. Dujardin, Modelling and optimization of IR cell devoted to in situ and operando characterization of catalysts, Catal. Today. 205 (2013) 134–140, https://doi.org/10.1016/j.cattod.2012.08.003.